Elevated synaptic PKA activity and abnormal striatal dopamine signaling in *Akap11* mutant mice, a genetic model of schizophrenia and bipolar disorder

Bryan J. Song[1, #,*], Yang Ge[1,*], Ally Nicolella[1], Min Jee Kwon[1], Bart Lodder[2,3], Kevin Bonanno[4], Antia Valle-Tojeiro[4], John Adeleye[1], Chuhan Geng[1], Sahana Natarajan[1], Inès Picard[1], Nate Shepard[1], Sameer Aryal[1], Zohreh Farsi[1], Xiao-Man Liu[1], Nader Morshed[1,5], Naeem M Nadaf[1], Kira Perzel Mandell[1], Horia Pribiag[1], Sean K Simmons[1], D.R. Mani[4], Beth Stevens[1,5,6], Evan Z. Macosko[1,7], Joshua Z. Levin[1], Bernardo L. Sabatini[3,8], Hasmik Keshishian[4], Steven A. Carr[4], Borislav Dejanovic[1,9], Adam J. Granger[1,#] & Morgan Sheng[1,10,#]

1 The Stanley Center for Psychiatric Research, The Broad Institute of MIT and Harvard, Cambridge, MA, USA
2 Brain Center, Department of Translational Neuroscience, University Medical Center Utrecht and University Utrecht, the Netherlands
3 Department of Neurobiology, Harvard Medical School, Boston, MA, USA
4 The Proteomics Platform, The Broad Institute of MIT and Harvard, Cambridge, MA, USA
5 F.M. Kirby Neurobiology Center, Boston Children's Hospital, Boston, MA, USA
6 Howard Hughes Medical Institute, Boston Children's Hospital, Boston, MA, USA
7 Massachusetts General Hospital, Department of Psychiatry, Boston, MA, USA
8 Howard Hughes Medical Institute, Harvard Medical School, Boston, MA, USA
9 Currently: Vigil Neuroscience, Cambridge, MA, USA
10 Department of Brain and Cognitive Sciences, Massachusetts Institute of Technology, Cambridge, MA, USA
* Equal Contributions
# Correspondence: msheng@broadinstitute.org, agranger@broadinstitute.org, bsong@broadinstitute.org

Abstract

Loss-of-function mutations in *AKAP11* (a protein kinase A (PKA)-binding protein) greatly increase the risk of bipolar disorder and schizophrenia. We conducted multi-omic analyses of *Akap11* mutant mouse brains and report the neurobiological functions of AKAP11 and the consequences of its absence. AKAP11 interacts with multiple proteins involved in signaling and proteostasis. In *Akap11*$^{+/-}$ and *Akap11*$^{-/-}$ synapses, PKA protein levels were markedly elevated, and many synaptic proteins were hyperphosphorylated at PKA substrate sites. *Akap11* mutant brains showed extensive transcriptomic changes, prominently in synapse-related gene-sets and most profoundly in neurons of the striatum, a brain region implicated in motivation, cognition and psychiatric disorders. *In vivo*, real-time measurements of PKA activity in *Akap11*$^{-/-}$ revealed constitutively elevated kinase activity, which distorts the dynamic range of dopamine to PKA signaling in the striatum. Our work reveals the molecular basis of circuit dysfunction in a genetically valid model of psychotic disorder.

Introduction

Bipolar disorder (BD) and schizophrenia (SCZ) are debilitating psychiatric conditions within the psychosis spectrum whose biological basis remains unknown. Recent exome sequencing studies of case-vs.-control human populations have discovered multiple genes in which rare loss-of-function mutations greatly increase the risk for SCZ[1] and BD[2]. These rare genetic

variants with large impact (odds ratio, 3-40) offer an inroad into disease mechanisms, in part by enabling the creation of animal models with human genetics validity[3–5].

Mutations in *AKAP11* (A-kinase anchoring protein 11) are associated with elevated risk of both SCZ and BD[1,2,6]. Unlike some other SCZ risk genes, *AKAP11* has not been associated with autism spectrum disorder, epilepsy or intellectual disability[2] and therefore is a relatively specific risk gene for the SCZ-BD psychotic disorder spectrum. In our previous neurophysiologic study, we reported that *Akap11* loss-of-function mutant mice recapitulate several electroencephalogram (EEG) abnormalities found in schizophrenic patients, including increased power of resting gamma oscillations, non-rapid eye movement (REM) sleep reduction, and gene-dose-dependent reduction in sleep spindles[7]. The molecular and cellular mechanisms by which *Akap11* deficiency results in brain network dysfunction has not been studied.

The *Akap11* gene encodes a member of the A-Kinase anchoring proteins (AKAPs), which bind Protein Kinase A (PKA) and are typically localized to compartments within a cell, targeting PKA to a subcellular domains[8]. In non-neuronal cell lines, AKAP11 is reported to localize to punctate structures, including multivesicular bodies[9] and peroxisomes[10]. In addition to PKA, AKAP11 is reported to interact biochemically with the protein kinase GSK3β[11], Protein Phosphatase 1[12], IQGAP1[13], $GABA_C$ receptors[14], and vesicle-associated proteins A and B (VAPA, VAPB)[15], each of which is implicated in signaling and trafficking pathways that influence synaptic plasticity and neuronal development. Intriguingly, AKAP11 not only binds but inhibits the activity of GSK3β[11], a target of the mood-stabilizing drug lithium that is used to treat BD. AKAP11 also functions as an autophagy receptor for the regulatory subunit 1 of PKA (*Prkar1a*) which promotes protein-level degradation of PRKAR1α in the context of cellular stress[16]. Because AKAP11 has not been studied in the brain, there is insufficient knowledge to bridge the cell biology of *AKAP11* and psychiatric disease risk. In this study, we use unbiased multi-omic approaches to explore the consequences of *Akap11* loss-of-function across widespread brain regions and cell types, spanning several postnatal ages, within synaptic compartments, and in the context of dopaminergic signaling, followed by *in vivo* fiber photometry measurements of PKA activity. Our data uncover a fundamental role of *AKAP11* in synapse function and highlight the striatum as a nexus of circuit dysfunction in a model of psychosis risk with human-genetics validity.

Results

Identifying the AKAP11 interactome in brain

Little is known about AKAP11 in the brain, so we characterized the protein interactome of AKAP11 by immunoprecipitation of AKAP11 from cortical extracts followed by mass spectrometry (coIP-MS, Fig. 1a,b, Extended Data Fig. 1a). Of the ~2000 proteins identified by mass spectrometry, 68 proteins were enriched ($P < 0.05$) in AKAP11 coIP from *Akap11* wild-type (WT) cerebral cortex versus coIP from negative control *Akap11*$^{-/-}$ (knockout) mice[17]; these were considered specific interactors of AKAP11 (Fig. 1c; Supplementary Table 1). This approach yielded putative AKAP11-associated proteins that were largely overlapping with those found by comparison of AKAP11 coIP vs control IgG coIP from WT brains (Extended Data Fig.

1b). Of the 68 proteins that were most associated with AKAP11 in the brain, only 7 were previously reported in cell lines or other tissues, including PKA subunits, GSK3β, and VAPA and VAPB (Fig. 1d)[11,15]. The biochemical association of AKAP11 with PKA catalytic and regulatory subunits and several other interactors (VAPA, VAPB, GSK3β, DRYK1A) was confirmed by coIP-immunoblot experiments (Fig. 1e-j). AKAP11 did not associate with the cytoskeleton protein Vinculin, indicating specificity for the above results (Fig. 1e).

As expected for an AKAP protein[8], we observed the greatest enrichment of multiple subunits of PKA in AKAP11 immunoprecipitates (Fig. 1c, e). PKA exists as a tetrameric holoenzyme with regulatory subunits that bind and suppress the kinase activity of catalytic subunits. Within AKAP11 coIPs there was greater degree of enrichment for regulatory subunits PKA R1α and PKA R1β (encoded by *Prkar1a* and *Prkar1b*) than the catalytic subunits PKA Cα, PKA Cβ (encoded by *Prkaca* and *Prkacb*), which is consistent with AKAP11 directly binding to regulatory subunits of PKA[18]. Adenylyl cyclase 10 (encoded by *Adcy10*) was also enriched, and this enzyme produces cyclic AMP, the signaling molecule that activates PKA. There was only modest enrichment for type 2 regulatory subunits (PKA R2α, PKA R2β. Extended Data Fig. 1c) even though AKAP11 has high affinity binding sites for R2[18]. We confirmed that AKAP11 also associates with GSK3β in the brain, consistent with prior studies in cell lines[11,18,19] and did not detect an association with GSK3α (Fig. 1h).

Our coIP-MS experiments uncovered multiple novel interactors of AKAP11 including DYRK1A, SPHKAP, SV2B and P62 (Fig. 1c,d). By coIP-immunoblot, we confirmed AKAP11 binding to DYRK1A (Fig. 1i, j), a tyrosine kinase that is genetically linked to autism spectrum disorders[20] and is implicated in neurodevelopment, neurogenesis and neurite outgrowth[21–24]. We also explored the AKAP11 interactome by coIP from the brains of *Akap11*$^{+/-}$ (heterozygote) mutants, which mimics the human heterozygous genotype that is associated with greatly increased risk for SCZ/BD[2]. Proteins coIP'd with AKAP11 were largely similar in WT and *Akap11*$^{+/-}$ (Extended Data Fig. 1d,e).

To gain further insight into molecular pathways in which AKAP11 might play a role, we conducted gene-set enrichment analysis (GSEA)[25] on AKAP11-associated proteins (Fig. 1k, Supplementary Table 2). In addition to expected gene ontology (GO) pathways like "Phosphorylation", pathways enriched among AKAP11-associated proteins included "Spliceosomal Complex" and "Secretory Vesicle" (Extended Data Fig. 1f). Disturbed RNA splicing and misdistribution of RNA binding proteins are implicated in multiple brain disorders[26]. The "Secretory Vesicle" GO term includes Synaptic Vesicle Protein 2B (SV2B), involved in vesicular recycling[27], VAMP-associated Proteins A and B (VAPA/VAPB), endoplasmic reticulum (ER) resident proteins that facilitate inter-organelle contact and vesicular transport, and SPHKAP, which interacts with VAP proteins near synapses to regulate calcium signaling from ER stores[28]. Most notably, we observed enrichment in AKAP11 coIP of the "Ubiquitin like protein ligase binding" GO term, which includes the selective autophagy receptor P62 and RPL40 (encoded by *Uba52*) (Extended Data Fig. 1f). In cell lines, AKAP11 interacts with autophagosomes, intracellular vesicular structures involved in protein degradation[29], possibly through the selective autophagy receptor LC3[16]. In our coIP experiments, we found an

association of AKAP11 with P62, but not LC3 (Extended Data Fig. 1c), suggesting that in the brain, AKAP11 also interacts with autophagosomes but possibly by distinct molecular mechanisms.

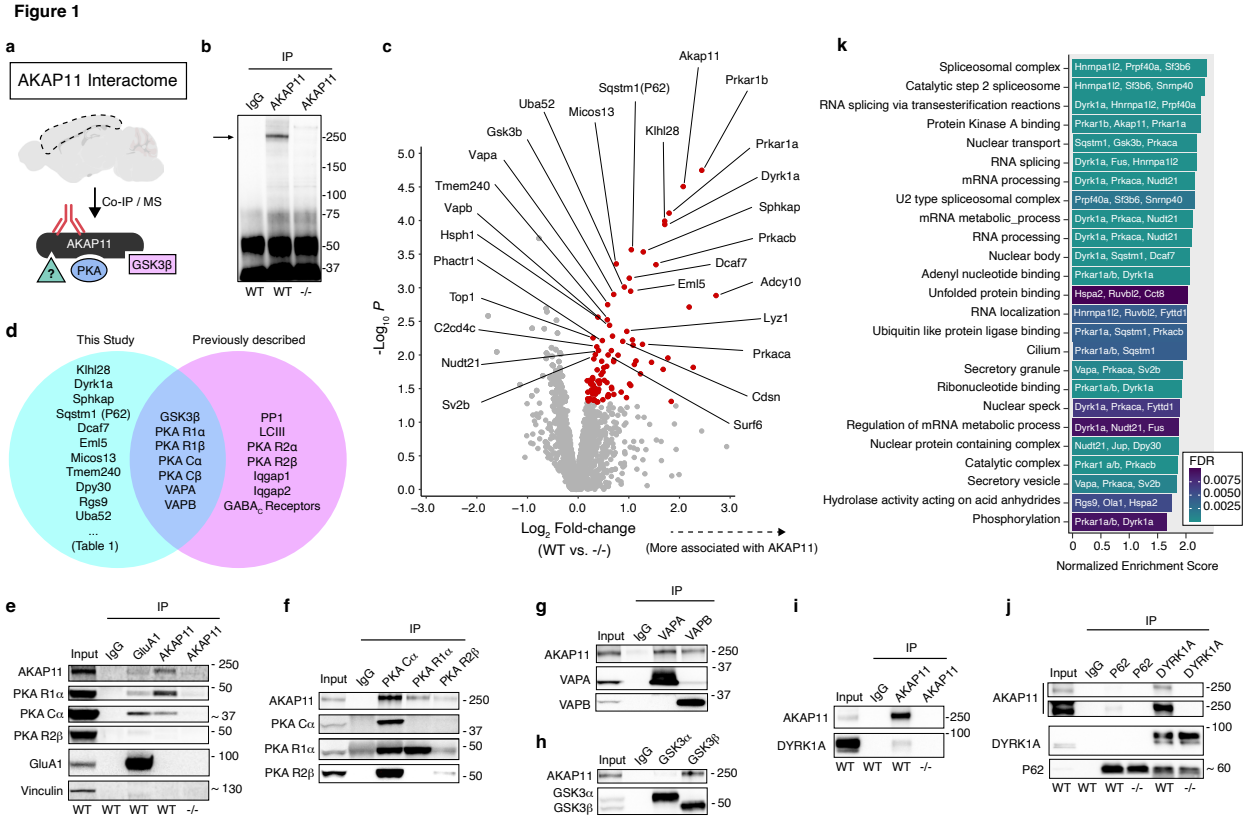

Figure 1: Characterization of the AKAP11 interactome in the brain.

a) Schematic of AKAP11 immunoprecipitation (IP) and its most notable, known interactors.

b) Immunoblot of AKAP11 in IPs of anti-AKAP11 and control IgG in 12-week-old wild-type (WT) or *Akap11*$^{-/-}$ cortical tissue.

c) Volcano plot comparing Log_2 Fold-Change (Log_2FC) against *P* value for AKAP11 IP in WT vs *Akap11*$^{-/-}$, displaying all proteins detected by coIP-MS. Proteins that were enriched (red) by anti-AKAP11 IP from WT versus *Akap11*$^{-/-}$ cortical extracts. Enriched proteins, defined by having a nominal *P* value < 0.05 and Log_2FC > 0, are colored red. Downregulated proteins are mostly antibody-related artifacts and can be found in Supplementary Table 1).

d) Venn diagram comparing previously published AKAP11 interactions with the brain interactome in this study. Full results are displayed in Supplementary Table 1.

e) Immunoblot of AKAP11, PKA subunits and control proteins, in IPs of AKAP11, GluA1 or IgG control in WT or *Akap11*$^{-/-}$ cortical lysate.

f) Immunoblot of AKAP11 in IPs of PKA subunits, in WT cortical lysates.

g-j) Immunoblot with indicated antibodies, in IPs of anti-GSK3α, GSK3β, VAPA, VAPB, AKAP11, P62 or DYRK1a in WT or *Akap11*$^{-/-}$ cortical lysate.

k) Gene set enrichment analysis of all proteins displayed in 1c, showing selected gene ontologies with a positive normalized enrichment score (NES) and adjusted *P*-value (FDR) < 0.01. Redundant (similar) pathways were removed for clarity. Full results are available in Supplementary Table 2. The top most enriched proteins within each ontology are listed within the histograms.

Accumulated PKA in *Akap11* mutant mice

Individual components of a protein interaction network can regulate the activity or turnover/stability of their binding partners. What happens to AKAP11 protein interactors when the AKAP11 scaffold protein is lost? By immunoblotting of total cortical lysate, we found a striking elevation of PKA protein levels (regulatory (~6x) and catalytic (~9x) subunits in *Akap11*$^{-/-}$ mice) (Fig. 2a, Extended Data Fig. 2a). The association of AKAP11 with P62 in the brain (Fig.1c) suggests the possibility that AKAP11 regulates degradation of PKA by receptor-mediated selective macroautophagy, which has also been observed in cell lines[16,30,31]. Levels of other interactors, such as GSK3β, VAPA/B, P62 and DYRK1A were not substantially altered in *Akap11* mutant brains.

The marked elevation of PKA subunits in *Akap11*$^{-/-}$ mice was apparent at all ages examined (4, 12, 28 weeks of age, Fig. 2b). PKA subunits were not only increased in the cortex, but across all brain regions examined: prefrontal cortex (PFC), somatosensory cortex (SSC), striatum (Str), hippocampus (Hipp), thalamus (Thal) and substantia nigra (SN) (Fig. 2c). Compared with the multiple-fold increases in the homozygous (*Akap11*$^{-/-}$) mutant, changes in PKA protein levels in the heterozygous (*Akap11*$^{+/-}$) mutant brain were much more modest (Fig. 2a-c). Nonetheless, comparison with WT animals showed that PKA R1α and Cα subunits were consistently elevated by 20%-75% in *Akap11*$^{+/-}$ (Extended Data Fig. 2b,c). In the course of these immunoblotting experiments, we noted that levels of AKAP11 protein itself were reduced by much less than 50% in heterozygous (*Akap11*$^{+/-}$) mutants (Figs. 2a-c, Extended Data Fig. 2a,d), despite gene-dose dependent reduction of *Akap11* RNA (Extended Data Fig. 2e). This pattern is suggestive of posttranscriptional homeostatic compensation of *Akap11* expression when just one copy of the *Akap11* gene is deleted, and might explain the relatively modest effect on PKA in *Akap11*$^{+/-}$ vs. *Akap11*$^{-/-}$. Quantitative immunofluorescence imaging of PKA R1α protein in brain sections showed increased intensity across all brain regions of *Akap11*$^{-/-}$ mice (Extended Data Fig. 2f). Level of *PKA R1α* RNA was not significantly altered in *Akap11*$^{-/-}$ (Extended Data Fig. 2g), suggesting that AKAP11 regulates the stability or turnover of PKA at the protein level.

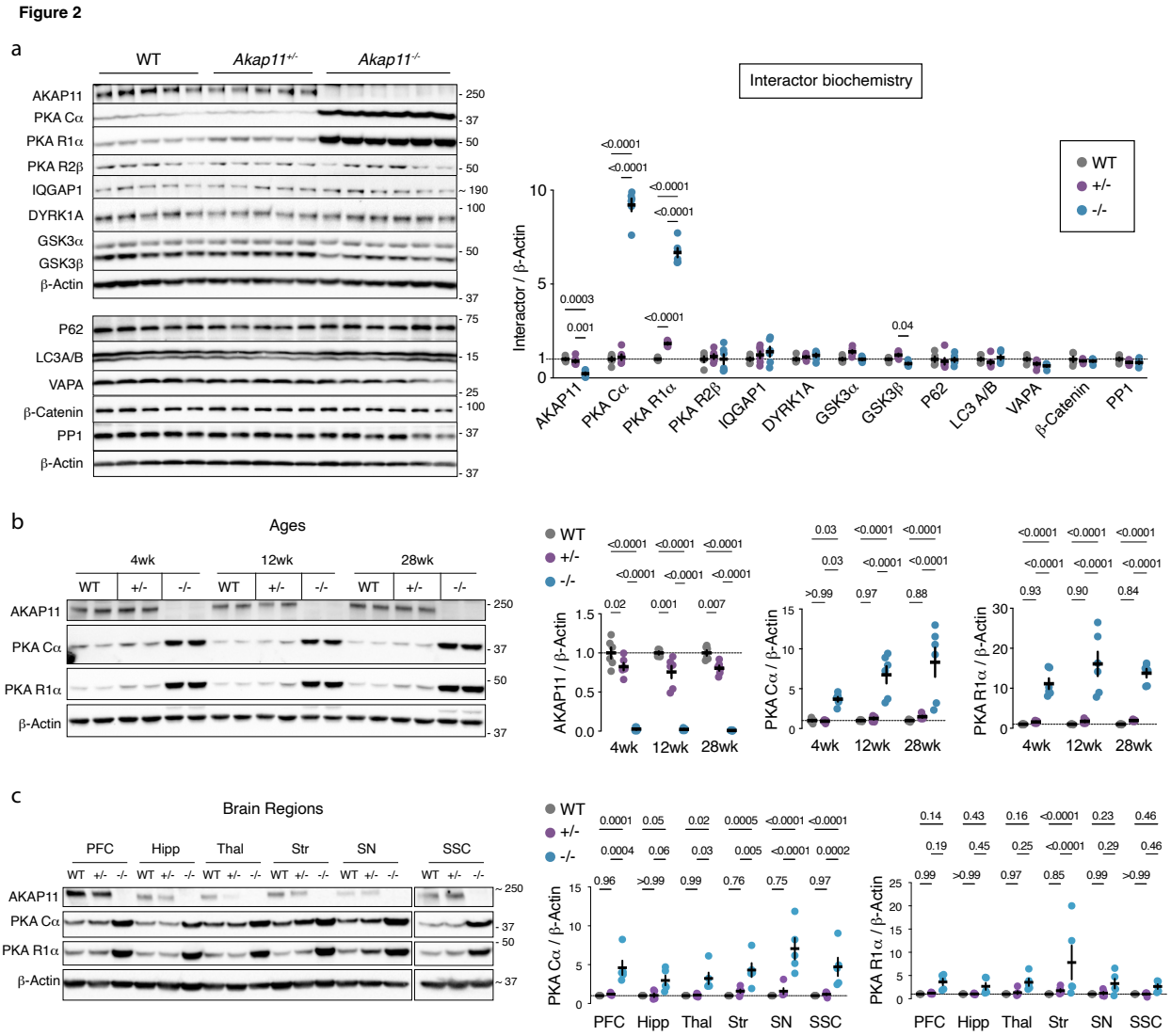

Figure 2. PKA protein levels are elevated across brain regions and ages of *Akap11* mutant mice.
a) Immunoblots and quantifications of 12wk cortex using antibodies against AKAP11-interacting proteins. Measurements are normalized to B-Actin and to WT controls for each antibody. $P < 0.05$ comparisons are shown.
b) immunoblots and quantifications of 4wk, 12wk and 28wk cortex using antibodies against AKAP11 and PKA subunits. Measurements are normalized to β-Actin and to WT controls within an age group.
c) Immunoblots and quantifications from microdissected tissue from 4wk mice using antibodies against AKAP11 and PKA subunits. Measurements are normalized to β-Actin and to WT controls within a region.
a-c) Data are represented as mean +/- SEM. Two-way ANOVA with Tukey's post hoc test.

Synapse protein changes and elevated PKA in AKAP11 deficient mice

PKA plays a key role in regulation of synaptic plasticity[32]. To understand the consequences of *Akap11* deficiency and PKA elevation in synapses, we investigated protein changes in purified synaptic (postsynaptic density, PSD) fractions of *Akap11* mutant mice by quantitative mass spectrometry-based proteomics and phosphoproteomics using Tandem Mass Tag (TMT) labeling reagents (see methods). Since the onset of SCZ often occurs in adolescence and early

adulthood[33], we examined 4 week (juvenile) and 12 week (young adult) animals. ~9000 proteins were identified in the PSD fraction purified from cortex, including AKAP11 itself which was modestly (~2x) enriched in the PSD fraction (Extended Data Fig. 3a,b). Differentially abundant proteins (DAPs, nominal $P < 0.05$) were more numerous in *Akap11*$^{-/-}$ than *Akap11*$^{+/-}$ mutants at 12 weeks but similar at 4 weeks, with a similar proportion of upregulated and downregulated DAPs overall (Fig. 3a, Supplementary Table 1). The DAPs were well correlated between *Akap11*$^{+/-}$ and *Akap11*$^{-/-}$ genotypes (Extended Data Fig. 3c) and weakly correlated between 4 and 12 weeks (Extended Data Fig. 3d).

In *Akap11*$^{-/-}$ synapses, the catalytic subunits PKA Cα and PKA Cβ were the two most upregulated proteins, at both 12 weeks (Fig. 3b) and 4 weeks, with PKA regulatory subunits also upregulated to a lesser extent (Extended Data Fig. 3e,f). Immunoblotting confirmed strong accumulation of PKA Cα (~5x) and R1α subunits (~2-3x) in homozygous *Akap11*$^{-/-}$ PSD fractions (Fig. 3c) and modest elevation of PKA Cα and PKA R1α (~1.2x -1.6x) in heterozygous *Akap11*$^{+/-}$ synapses (Extended data Fig. 3g). Besides PKA, many proteins showed changes in *Akap11*$^{-/-}$ synapse proteomics. Levels of SIK2, a PKA-regulated kinase involved in mood and circadian rhythms[34] and ARHGAP20, a Rho GTPase-activating protein[35], were significantly decreased in *Akap11*$^{-/-}$ synapses, at both 4 weeks and 12 weeks (Fig. 3b, Extended data Fig. 3e,f). Notably, levels of AKAP11 itself were significantly decreased in *Akap11*$^{+/-}$ synapse fractions (Fig. 3b,c; Extended Data Fig. 3e), which is in contrast to levels of AKAP11 in *Akap11*$^{+/-}$ crude lysate, which was more similar to WT levels (Fig. 2; Extended Data Fig. 2).

GSEA analysis of the synapse proteomic changes (Fig. 3d, Supplementary Table 2) revealed parallels to the pathways prioritized by GO analysis of the AKAP11 interactome (Fig. 1k). Translation- and mRNA/RNA processing-related pathways were downregulated (e.g. cytoplasmic translation, ribosome, cytoplasmic stress granule) (Fig. 3d), raising the possibility that altered local translation could affect synapse proteome composition of *Akap11* mutants. At 4 weeks, “Vesicle tethering complex” and “Ubiquitin ligase complex” processes were upregulated (Fig. 3d, Extended Data Fig. 3h), which bears resemblance to changes in synapses purified from BD and SCZ human brain tissues[36]. These findings may relate to our observation that AKAP11 interacts with proteins involved in ER-Golgi transport and proteostasis (Fig. 1c, k). We further examined the precise ontologies of DAPs using SynGO[37] to dissect the “sub-synaptic” processes that are altered in *Akap11* mutant synapses (Fig. 3e). DAPs in *Akap11*$^{-/-}$ mutant synapses were represented among pathways such as “Postsynaptic modulation of chemical transmission”, and “Postsynaptic neurotransmitter receptor endocytosis”. Relatedly, proteins in the “Clathrin coat” gene ontology were downregulated in 4wk and 12wk Akap11$^{+/-}$ synapse proteomes (Extended Data Fig. 3i). The same major pathways were represented amongst *Akap11*$^{+/-}$ DAPs, but to a lesser degree (Fig. 3e). Synaptic DAPs in *Akap11*$^{-/-}$ included Neuregulin 1 (NRG1) which has been genetically associated with SCZ and BD in family studies[38,39] and the D1 subtype dopamine receptor (DRD1) (Fig. 3e).

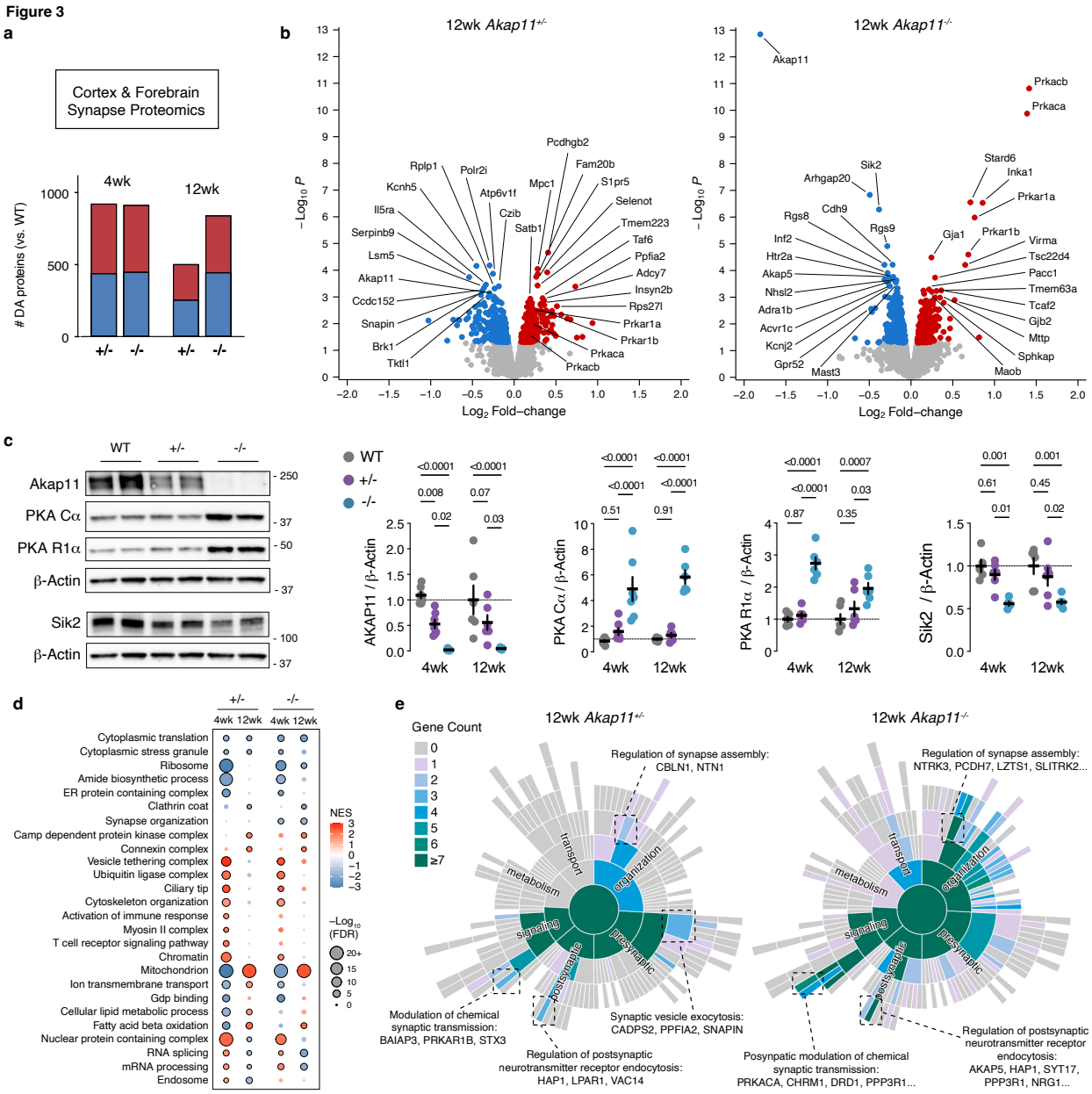

Figure 3: PKA accumulates in synapses of *Akap11* mutant mice

a) Number of DAPs across different ages and genotypes in synapse proteomics. Shading indicates upregulated (red) and downregulated (blue) DAPs, respectively. 4wk synapse proteomics data also appears in (Aryal et al., 2023)[36].

b) Volcano plots of 12wk synapse proteomics in *Akap11* mutants relative to WT. Upregulated and downregulated DAPs are colored red and blue, respectively.

c) Immunoblotting of synapse fractions with antibodies against AKAP11, PKA subunits, and SIK2. Right, quantifications for 4wk and 12wk animals. Data are represented as mean +/- SEM. Two-way ANOVA with Tukey's post hoc test.

d) A selection of GSEA analysis of synapse proteomics. Pathways displayed were significant at FDR < 0.05 in at least two age/ genotype conditions.

e) Sunburst plots showing SynGO Biological Process pathways and the number of $P < 0.05$ proteins within these ontologies. For selected ontologies, representative DAPs in the ontology are shown.

Hyperphosphorylation of synapse proteins in *Akap11* mutant mice

Within *Akap11*$^{-/-}$ synapses, the level of several protein kinases and phosphatases were altered, most obviously the accumulation of PKA catalytic subunits Cα and Cβ (Fig. 3b, c, Extended Data Fig. 3e). To quantify any phosphorylation changes in synaptic proteins in unbiased fashion, analyzed PSD fractions purified from *Akap11* mutant cortex by quantitative phosphoproteomics. *Akap11* mutants showed a large number of differentially abundant phosphoproteins (DAPPs, nominal $P < 0.05$), which was higher in *Akap11*$^{-/-}$ than *Akap11*$^{+/-}$, and higher at 4 weeks than 12 weeks (Fig. 4a, Extended Data Fig. 4a, Supplementary Table 1). We mapped changes in the synapse phosphoproteome against a reference of known and predicted kinase effectors[40] to infer the kinases responsible. The vast majority of PKA phospho-substrates detected in the synapse phosphoproteomes data were increased in *Akap11*$^{-/-}$ and a number of these phosphoproteins were also highly upregulated in *Akap11*$^{+/-}$ (Fig. 4b). The sequences flanking the phosphosites showed strong enrichment of the basophilic RRXS*/T* motif, particularly in the upregulated DAPPs of *Akap11*$^{-/-}$ synaptic fractions at both 4 and 12 weeks (Fig. 4c), which matches the consensus amino acid sequence that is preferred for phosphorylation by PKA[41]. Together, the synapse proteomics and phosphoproteomics data clearly show that PKA kinase activity as well as protein levels are abnormally elevated in the synapses of *Akap11* mutant mice.

Post-Translational Modification Signature Enrichment Analysis (PTM-SEA), which measures enrichment of kinase substrate sets (akin to GSEA using GO terms)[42], also indicated elevation of phosphorylated PKA substrates in A*kap11*$^{-/-}$, and to a lesser degree, *Akap11*$^{+/-}$ synapses (Fig. 4d). Phosphorylation of substrates by CaMK2A, a kinase involved in synaptic potentiation[43] was significantly downregulated in *Akap11*$^{-/-}$ synapses at 12 weeks. Since AKAP11 is reported to inhibit GSK3β, it was intriguing to find that phosphorylation of *β*-Catenin (a well-known GSK3β substrate, encoded by *Ctnnb1*) was increased at Ser37 in *Akap11* mutants[44,45] (Extended Data Fig. 4b). Phosphorylation of GSK3β itself on S9, a PKA phosphosite that regulates GSK3β activity[46], was significantly elevated in *Akap11* mutants (Fig. 4e). Regulation of brain GSK3β by *Akap11* is interesting because lithium, an inhibitor of GSK3, is a mainstay treatment of BD[47] and GSK3β overactivity has been implicated in SCZ animal models[48].

Most notably, among the most highly changed phosphoproteins in *Akap11*$^{-/-}$ synapses was AMPA receptor subunit GluA1 (*Gria1*), which is phosphorylated by PKA at S845 (annotated as S863 in the UniProt mouse reference; Fig. 4b,f, Extended Data Fig. 4a,d). Phosphorylation of GluA1 at S845 is a well-known correlate of AMPA receptor trafficking to the synapse[49–53]. We confirmed by immunoblotting that GluA1^{S845} phosphorylation was sharply increased (~4x) in brain lysates of *Akap11*$^{-/-}$ mutants, while total GluA1 protein showed little change (Fig. 4f, Extended Data Fig. 4d). Additional DAPPs in *Akap11*$^{-/-}$ synapses that are known to be regulated by PKA include Snap25^{T138}, a phosphosite required for presynaptic vesicular release[54] and RIM1^{S413}, phosphorylation of which is induced during synaptic potentiation[55–57] (Fig. 4b). In *Akap11*$^{+/-}$, PKA substrate DAPPs included RIMS1^{S413} and ITPR2^{S937}, a phosphosite that regulates intracellular calcium release[58]. The strength of synaptic transmission is regulated in large part by dynamic phosphorylation of synaptic proteins, including postsynaptic glutamate

receptors subunits such as GluA1[59]. By mapping our phosphoproteomics data onto the phosphosites that are induced with chronic neuronal activation or silencing[59], we found that many phosphosites associated with upscaling or downscaling of synaptic strength were also highly changed in *Akap11* mutants (Extended Data Fig. 4c), reflecting potential changes in synaptic function.

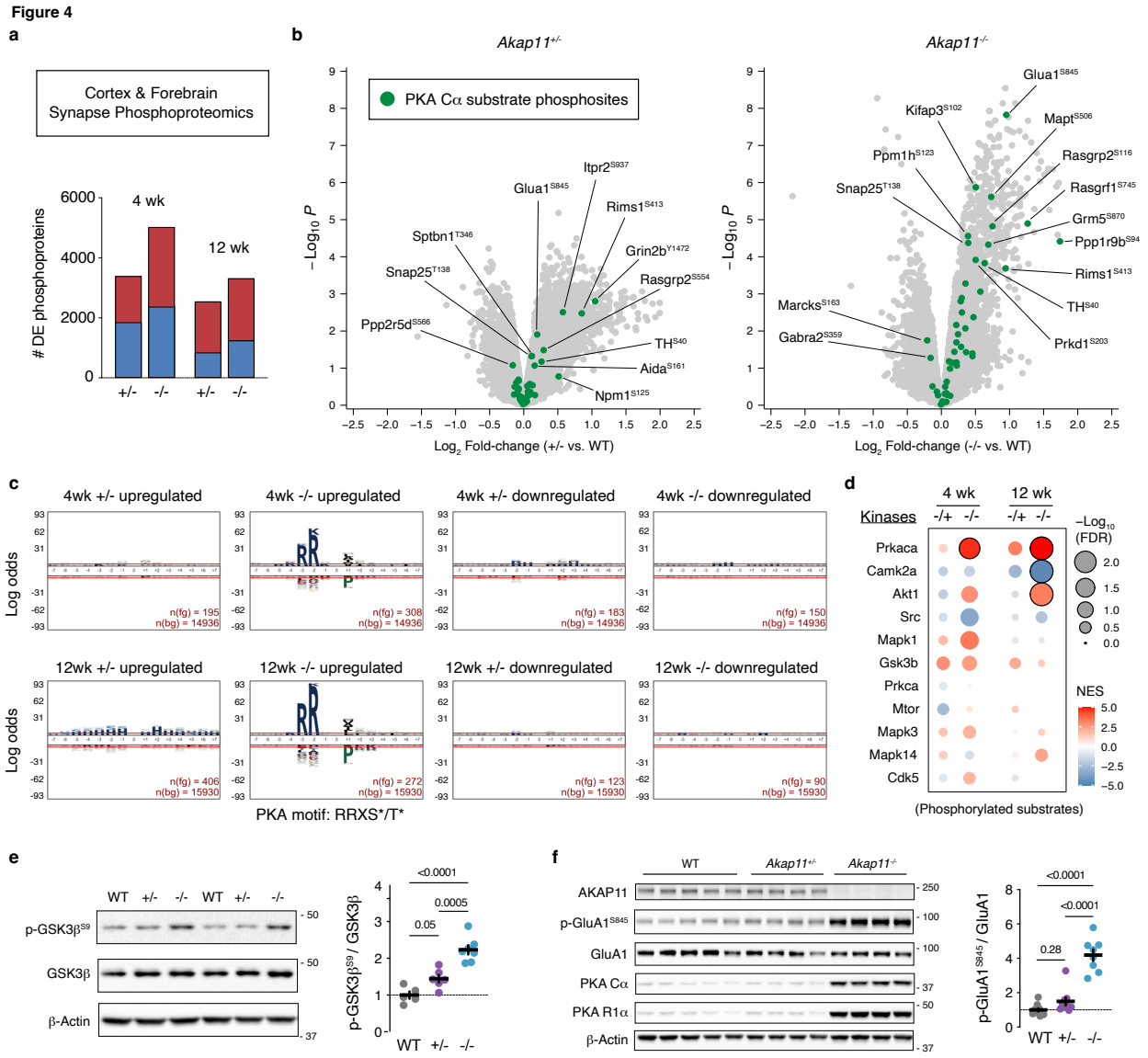

Figure 4: Phosphoproteomics of *Akap11* mutant synapses shows hyperphosphorylation of PKA substrates

a) Number of phosphoproteins reaching a significance threshold of nominal $P < 0.05$. Fractions of upregulated and downregulated DAPPs are highlighted in red and blue respectively.

b) Volcano plots of 12wk synapse phosphoproteomics data for *Akap11*$^{+/-}$ and *Akap11*$^{-/-}$ vs. WT controls. Phosphoproteomic measurements are normalized to MS-proteomics measurements from the same samples. Known PKA Cα substrates from PhosphoSitePlus are labeled green. AKAP11 phosphopeptides are omitted from *Akap11*$^{-/-}$ plots, for clarity.

c) Motif analysis of peptides flanking the phosphorylation site of $P<0.05$ phosphosites in A. n(fg) are the number of foreground peptides, and n(bg) are the number of background peptides. Red lines indicate FDR significance.

d) PTM-SEA of synapse phosphoproteomics data, using known kinase substrates from PhosphoSitePlus. Black borders indicate FDR significance.
e) Immunoblotting and quantification of p-GSK3β^{S9} and GSK3β in 4wk cortical lysate.
f) Immunoblotting and quantification of AKAP11, PKA subunits, p-GluA1^{S845} and GluA1 in 12wk cortical lysate.
e,f) Data are represented as mean +/- SEM. One-way ANOVA with Tukey's post hoc test.

Aberrant synaptic function in *Akap11* mutants

To directly examine synaptic function and plasticity in *Akap11* mutants, we performed electrophysiology recordings from acute hippocampal slices (6-8 week old mice). Under basal conditions, the stimulation input/output relationships (stimulation of Schaffer collaterals to CA1) of *Akap11*$^{-/-}$ mice were indistinguishable from WT (Extended Data Fig. 4e). The amplitude of early long-term potentiation (LTP) induced by theta burst stimulation (TBS) was modestly but significantly reduced in *Akap11*$^{-/-}$ mice (Extended Data Fig. 4f). We speculate this phenotype could be due to partial occlusion of LTP by hyperphosphorylated GluA1 at S845[52,60,61]. *Akap11*$^{-/-}$ slices also showed heightened paired-pulse facilitation (Extended Data Fig. 4g), suggesting reduced presynaptic release probability, which might relate to altered RIM1^{S413} and Snap25^{T138} phosphorylation seen in the synapse phosphoproteomics (Fig. 4b). The electrophysiologic phenotype in heterozygous *Akap11*$^{+/-}$ mice was generally not significantly different from WT, though there was a trend toward reduced magnitude of early LTP (Extended Data Fig. 4f).

Altered synaptic genes and striatal circuits revealed by spatiotemporal transcriptomic survey

Beyond AKAP11's biochemical and cellular functions, what are the brain region and circuit-level consequences of *Akap11* deficiency? *Akap11* mRNA is broadly expressed across the brain and across postnatal development in wild-type mice (Extended Data Fig. 5a). We conducted bulk RNA-seq on PFC, SSC, Str, Thal, Hipp, SN, as well as single-nucleus RNA sequencing (snRNA-seq) on PFC and Str, at 4 weeks and 12 weeks (Fig. 5a, Extended Data Fig. 5b,c) to query the circuits and molecular pathways that are impacted by *Akap11* loss of function. By bulk RNA-seq, we found more differentially expressed genes (DEGs; defined as genes that changed in either direction with FDR <0.05, Supplementary Table 3) in *Akap11*$^{-/-}$ than *Akap11*$^{+/-}$, and at 4 weeks than at 12 weeks of age (Fig. 5b). Based on DEG count, the most impacted regions in *Akap11*$^{-/-}$ were striatum, thalamus and PFC, whereas thalamus was the most affected in *Akap11*$^{+/-}$. The striatum had by far the most DEGs, at either age, in *Akap11*$^{-/-}$ (Fig. 5b). Only a few DEGs were common across brain regions (Extended Data Fig. 5d), and the correlation of Log_2-Fold-Changes of nominally significant genes was low between different brain regions, and modest between 4 and 12 weeks for the same brain region (Extended Data Fig. 5e). Thus the transcriptional consequence of *Akap11* mutation varies with the brain region and developmental context.

Notable DEGs that were changed across multiple brain regions and ages included *Entpd4*, which was diminished across all examined brain regions (Extended Data Fig. 5d) and encodes an autophagosome/lysosome-associated enzyme[62]; *Cacna1i* (Cav3.3 calcium channel), which was down in the striatum and thalamus of *Akap11*$^{-/-}$ and encodes a T-type calcium channel that

regulates sleep spindles[63,64], an EEG feature that is reduced in *Akap11* mutant mice and SCZ patients[7,65]. Interestingly, *Prkar1a* mRNA, encoding the R1α subunit of PKA, was significantly reduced in the PFC, SSC and thalamus of *Akap11*$^{-/-}$ mutants, perhaps as a compensatory response to increased PKA R1α protein level (Fig. 2a).

GSEA of bulk transcriptomic changes revealed major dysregulation of biological pathways related to synapses, mitochondria/oxidative phosphorylation, ribosomes, and RNA processing/splicing across most brain regions and ages (Fig. 5c,d, Supplementary Table 4). Synapse-related gene sets were among the most significantly changed GO terms across most brain regions and ages, particularly prominent in SN at 4wk (Fig. 5c,d). The strong enrichment of synapse-related genes in the transcriptomic changes of *Akap11* mutant mice reinforces the conclusion that synaptic organization, signaling, and function are profoundly impacted by *Akap11* deficiency (see above). The "synapse" pathway was consistently downregulated in PFC at both 4 and 12 weeks in *Akap11*$^{+/-}$ and *Akap11*$^{-/-}$ mutants (Fig. 5d). Synapse-related genes were upregulated in striatum at 4 weeks in *Akap11*$^{-/-}$, but downregulated in the SN, which sends dopaminergic input to the striatum (Fig. 5d). At 12 weeks, interestingly, this SN-striatum pattern of synaptic gene set dysregulation was reversed. Immune-related pathways were conversely upregulated in the 4wk SN, which is notable in the context of synaptic pruning by glia during development and disease[66] and SCZ patient associations with immune-related genetic loci[67,68]. Two pathways required for cellular energetics and upkeep, "Oxidative phosphorylation" and "Ribosome", were highly correlated, consistent with observations in another SCZ rare variant mouse model [3] and these pathways are also altered in human SCZ postmortem samples[69,70]. The "oxidative phosphorylation" pathway, a mitochondrial process that generates ATP for cells, was down in the PFC of 4 week *Akap11*$^{+/-}$ *and Akap11*$^{-/-}$ mutants and increased in the SSC (Fig. 5c,d). These ox-phos findings, together with the consistent downregulation of the "Synapse" GO term in PFC, is suggestive of selective hypofunction of PFC that is reported in fMRI studies of humans with SCZ and BD[71,72].

We next investigated changes to neuronal activity, at the systems-level, in the brains of *Akap11* mutant mice. As a surrogate measure of neuronal activity, we conducted GSEA of the bulk RNA-seq data using a curated set of activity-regulated genes (ARGs)[3,73]. Overall, ARGs were more changed at 4 weeks than at 12 weeks in *Akap11* mutants (Fig. 5e). At 4 weeks, the ARG gene-set trended downward in most brain regions, reaching significance in SSC (both *Akap11*$^{+/-}$ and A*kap11*$^{-/-}$) and in SN (A*kap11*$^{-/-}$). However, ARGs were notably upregulated in the hippocampus of *Akap11*$^{+/-}$ mice (4 weeks) and in striatum (reaching FDR significance in 4 week A*kap11*$^{-/-}$) (Fig 5e). By 12 weeks, ARG expression was largely normalized, aside from a significant upregulation in the PFC of *Akap11*$^{-/-}$ mice.

We queried the bulk RNA-seq changes in *Akap11* mutants for enrichment of SCZ- and BD-associated risk genes from human genome-wide association studies (GWAS) and other studies (Extended Data Fig. 5f). The pattern of GSEA results was similar for SCZ and BD risk genes, and were most enriched in the downregulated genes of the SN in both *Akap11*$^{+/-}$ *and Akap11*$^{-/-}$ mutants (Extended Data Fig. 5f). Besides SCZ and BD, we also observed similar GSEA signals for risk genes associated with ASD and neurodevelopmental disorders[20,74–76]. The same GSEA

analysis showed minimal enrichment of GWAS signals for neurodegenerative disorders, epilepsy or aging (Extended Data Fig. 5f). Overall, these results support that Akap11 functionally engages with other SCZ and BP and neurodevelopmental risk genes, and they are consistent with the known genetic overlap between SCZ, BP, and neurodevelopmental disorders (NDD)[1,77]. In the striatum of *Akap11*$^{-/-}$, the region with the most DEGs, there was enrichment of high confidence SCZ and BD GWAS genes[78,79] in the downregulated genes of striatum (Fig. 5f). In this context we note that expression of Grin2a, which has both rare variant (LoF) and common variant associations with SCZ, was reduced in *Akap11*$^{-/-}$ striatum bulk RNA (Fig 5f).

Figure 5

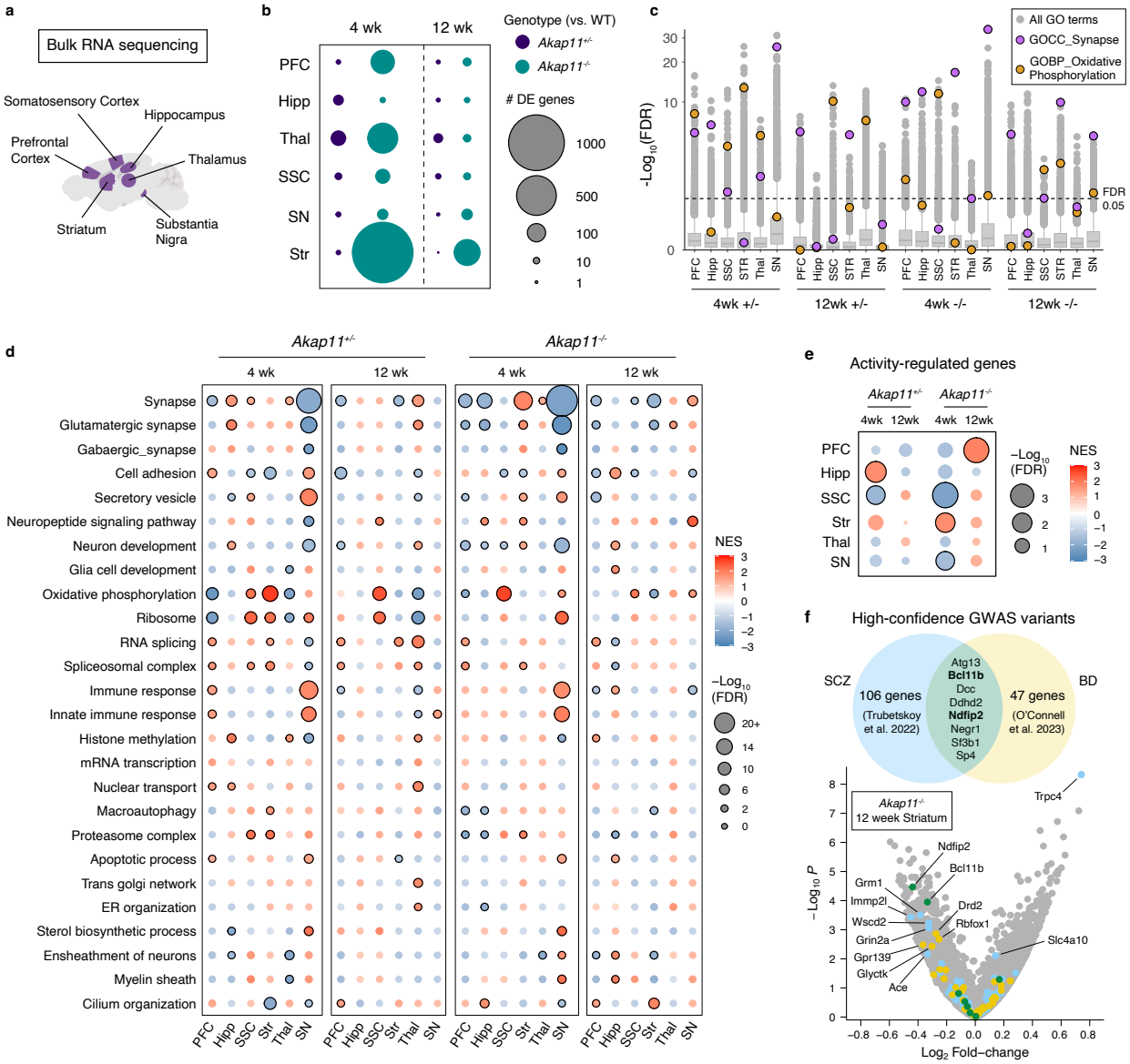

Figure 5: Transcriptome-wide impact of *Akap11* deficiency across brain regions at 4 weeks and 12 weeks.
a) Schematic of brain regions collected for bulk RNA sequencing.

b) Number of differentially expressed genes (DEGs) in bulk RNA sequencing across brain regions and ages. Area of circles represents DEG counts, defined by FDR adjusted *P*-values < 0.05, for *Akap11* mutants compared to WT controls.
c) Distributions of adjusted *P*-values (FDR) for each GO term across bulk RNA sequencing datasets. GO Cellular Component term "Synapse" and GO Biological Process term "Oxidative Phosphorylation" are highlighted in orange and blue, respectively.
d) GSEA of bulk RNA sequencing, showing MsigDB pathways of interest.
e) GSEA of bulk RNA sequencing using a curated set of activity-regulated genes.
f) Venn diagram of overlapping SCZ and BD GWAS genes prioritized by the Psychiatric Genetics Consortium[78,79]. Volcano plots of transcriptomic changes identified by bulk RNA seq analysis in 12wk striatum with these genes highlighted below.
d,e) Black outline indicates FDR < 0.05 significance.

Major disturbances to striatal neurons revealed by single nucleus RNA-seq

To investigate the effects of *Akap11* deficiency on specific brain cell types, we conducted single-nucleus RNA sequencing (snRNA-Seq) in the PFC and striatum at 4 and 12 weeks (Fig. 6a, Extended Data Fig. 6a). There were no major changes in cell type proportions in *Akap11* mutant PFC or striatum (Extended data Fig. 6a). In WT mice, *Akap11* mRNA is expressed in excitatory and inhibitory neurons in all brain regions, as well as in glia (Extended Data Fig. 6b). Though all cell types in PFC and striatum showed transcriptomic changes in *Akap11* mutants (Fig. 6b), the largest numbers of DEGs (FDR <0.05, Supplementary Table 5) were found in the major neuron-types of the striatum of *Akap11*$^{-/-}$, namely the inhibitory direct- and indirect-pathway spiny projection neurons (dSPNs, iSPNs) (Fig. 6b). Transcriptomic alterations in *Akap11*$^{-/-}$ mutants were highly correlated between iSPNs and dSPNs (Fig. 6c, Extended Data Fig. 6c, d) and between 4 and 12 weeks of age (Extended Data Fig. 6d,e). Consistent with bulk RNA-seq findings (Fig. 5b), *Akap11*$^{+/-}$ had much less effect than *Akap11*$^{-/-}$ on SPN in snRNA-seq (Fig. 6b, Extended Data Fig. 6d,f). Nearly all PFC neuron subtypes showed downregulation of the "Synapse" GO pathway (Fig. 6c, Supplementary Table 6), which aligns with our observations using bulk RNA-seq (Fig. 5d). Unlike striatal neurons, which are much more impacted by homozygous *Akap11* mutation, glia in the PFC and striatum (astrocytes, oligodendrocytes and microglia) showed comparable numbers of DEGs genes between *Akap11*$^{+/-}$ and *Akap11*$^{-/-}$ (Fig. 6b). *Akap11* mutant astrocytes showed downregulation of the "Sterol Biosynthesis" pathway, particularly in the 4 week *Akap11*$^{+/-}$ PFC and *Akap11*$^{-/-}$ striatum (Fig. 6d). Across regions, ages and genotypes, decreases in synapse gene expression often occurred alongside decreased expression of cholesterol biosynthesis genes in astrocytes (Fig. 6e), suggesting the possibility of discoordinated neuron-glia homeostatic programs, which has been observed in postmortem human SCZ patients[80].

Examination of the largest changes in the *Akap11* mutant SPNs highlighted several neuromodulatory systems, including serotonin (*Htr2a*, *Htr4*), adenosine (*Adora1*), acetylcholine (*Chat*, *Chrna3*), and dopamine (*Cartpt*) (Fig. 6f,g; Extended Data Fig. 6g). Intriguingly, the serotonin receptor HTR2A, which is a target of hallucinogenic drugs[81,82], was downregulated in both *Akap11*$^{+/-}$ synapse proteomics and snRNA-seq of striatum inhibitory neurons (Fig. 6g), and Htr4 was robustly downregulated in bulk RNA-seq of striatum and in snRNA-seq of striatal SPNs (Fig. 6f,g, Extended Data Fig. 6g). Adenosine receptor ADORA1, a G-protein coupled

receptor that inhibits cAMP production, was downregulated in *Akap11*$^{-/-}$ synapse proteomics as well as bulk RNA-seq and snRNA-seq data in striatum and SPNs. Choline acetyltransferase (*Chat*) was also prominently downregulated in the striatum of *Akap11*$^{-/-}$ (Fig. 6f, g). *Chat* participates in the synthesis of acetylcholine, and signaling through muscarinic acetylcholine receptors is implicated in SCZ pathophysiology[83,84].

Transcellular signaling factors *Epha10*, *Cdh9*, and *Igsf21* were among the most altered genes in the *Akap11*$^{-/-}$ striatum (Fig. 6e, f). *Epha10* is a receptor tyrosine kinase that acts as an axon guidance molecule[85,86]. *Cdh9,* which decreased consistently across proteomics and transcriptomics measurements of *Akap11*$^{-/-}$, is involved in calcium dependent cell-cell adhesion[87]. *Igsf1* deficiency has been linked to hypothyroidism[88,89], a disease associated with increased risk for depression and BD[90].

Dopamine is a fundamental neuromodulator in the striatum, and implicated in psychotic disorders[91]. We found several dopamine-related genes, proteins, and posttranslational modifications that were altered in *Akap11* mutants (Fig. 6g), including: (i) increased phosphorylation of tyrosine hydroxylase (TH) at S40, which positively regulates its dopamine biosynthesis activity[92,93]; (ii) reduction of protein and increased phosphorylation of dopamine receptor DRD1, (iii) increased phosphorylation of RASGRP2^{S116} in 12 week *Akap11*$^{-/-}$ synapses (Fig. 4b), which is consistent with enhanced DRD1 signaling[94] (iv) elevated MAO-B protein in synapse fractions, an enzyme that degrades dopamine, v) increased proportion of Drd2-*expressing* (Drd2^{+}) neurons in *Akap11*$^{+/-}$ relative to wild-type at 4 and 12 weeks (Extended Data Fig. 6h). One dopamine-regulated transcript, *Cart* (Cocaine- and amphetamine-regulated transcript)[95,96] was highly elevated in the *Akap11*$^{-/-}$ striatum (bulk RNA-seq) and in striatal SPNs and PFC excitatory neurons (snRNA-seq) (Extended Data Fig. 6i), which may reflect heightened dopamine signaling in striatum and in PFC of *Akap11* mutants.

Figure 6

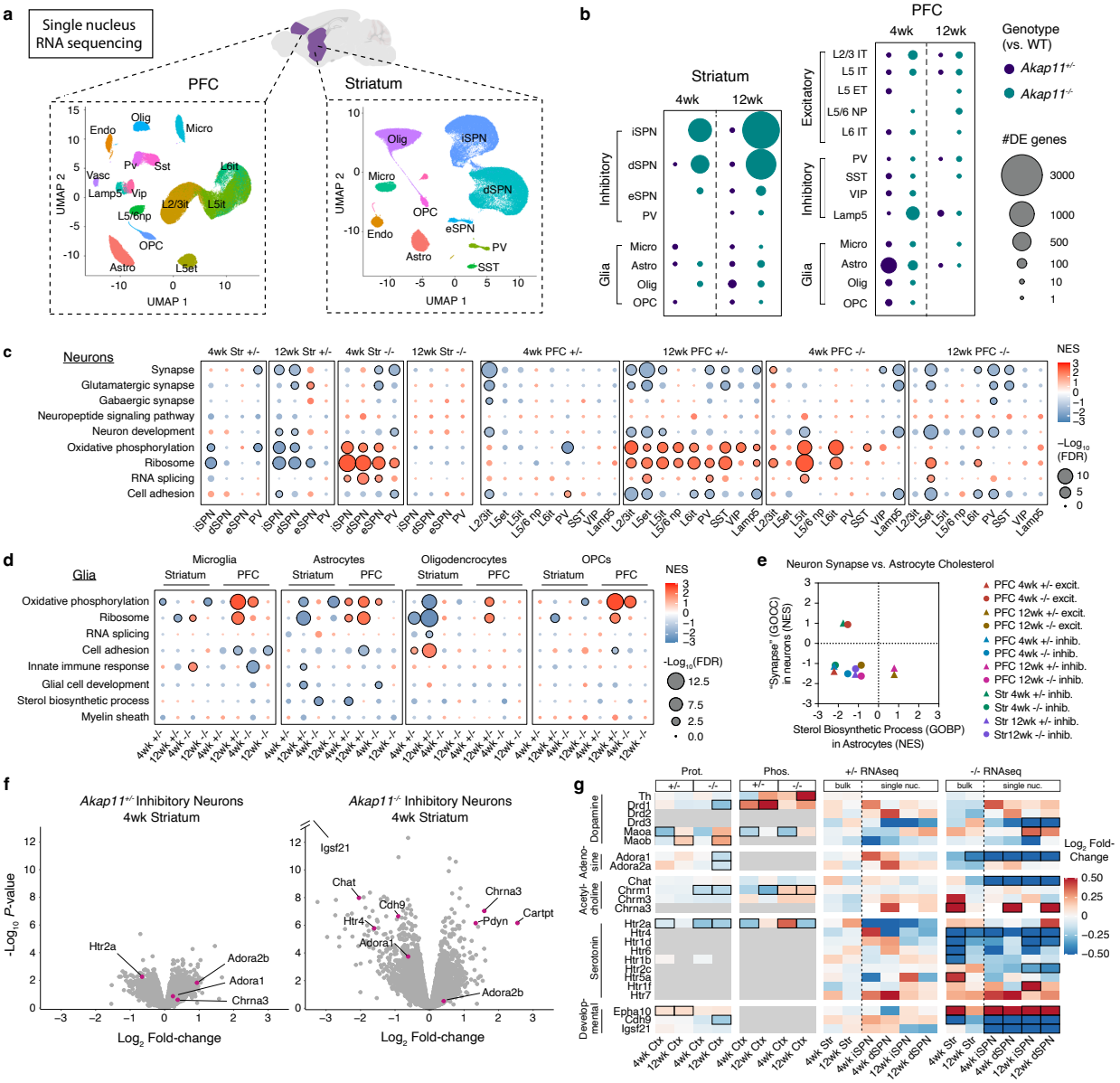

Figure 6: Cell-type specific transcriptomic impact of *Akap11* deficiency revealed by snRNA-seq.

a) Schematic of snRNA-seq experiments in PFC and striatum, with UMAP plots of major cell types identified at 12wk.

b) Number of DEGs in snRNA-seq experiments, defined by having an FDR adjusted *P*-value < 0.05.

c) GSEA from neurons identified by snRNA-seq of striatum and PFC, showing MsigDB pathways of interest.

d) GSEA results from glia snRNA-Seq, showing, showing MsigDB pathways of interest, including pathways related to glia function.

e) Comparison of NES from synapse pathways in neurons vs. cholesterol biosynthesis pathways in astrocytes.

f) Volcano plots of transcriptomic changes identified by snRNA-seq analysis in 4wk striatal inhibitory neurons. Genes of interest related to neuromodulation and circuit development are highlighted in magenta.

g) Heatmap showing Log_2FC values for a selection of neuromodulation-related genes, plotted across proteomics, phosphoproteomics, and transcriptomics measurements. Genes indicated in the phosphoproteomics columns reflect the most significantly changed phosphosite per gene. $P < 0.05$ proteins and FDR < 0.05 transcripts are outlined with a black box.

c,d) Black outline indicates FDR < 0.05 significance.

In vivo striatal PKA dynamics and dopamine signaling are regulated by AKAP11

The two most prominent phenotypes of *Akap11* mutant mice are highly elevated PKA protein (Figs. 2-4) and strong transcriptomic changes in the striatum and SPNs, the major neuron-type of striatum (Figs. 5 & 6). PKA has outsized importance in the striatum, acting as a key cytoplasmic effector in the signal transduction pathway downstream of dopamine receptors[91]. To assess real-time dynamics of PKA activity *in vivo*, we used fluorescent lifetime fiber photometry measurements of FLIM-AKAR, a fluorescent lifetime reporter of PKA activity[97,98] that was virally expressed in the nucleus accumbens (NAc), which is within the ventral striatum (Fig. 7a, Extended Data Fig. 7a,b). In awake, behaving mice, PKA activity of *Akap11*$^{-/-}$ mice was constitutively elevated across the recording session in an open field arena, indicated by the increased fluorescence lifetime of FLIM-AKAR (Fig. 7b) which was consistent across weeks of measurement (Extended Data Fig. 7c). As a negative control, there were no differences across *Akap11* genotypes in the lifetime of FLIM-AKAR^{T391A}, a mutated variant of FLIM-AKAR that is insensitive to PKA activity (Fig. 7c).

Dopamine receptors are enriched in the striatum, and excessive dopamine signaling in striatum is thought to contribute towards positive symptoms (e.g. hallucinations) of SCZ[99–101], which is supported by the clinical efficacy of dopamine receptor 2 (*Drd2*) antagonists for positive symptoms[102]. To evaluate how PKA dynamic responses to dopamine are influenced by *Akap11* deficiency, we administered dopamine receptor antagonists via intraperitoneal injection. Dopamine acting on D2-type receptors inhibits cAMP production and thereby inhibits PKA[91,103]. As expected, PKA activity was increased in striatal neurons following D2 antagonist administration (Fig. 7d). Despite the higher levels of baseline PKA activity in *Akap11*$^{-/-}$ striatum, the magnitude of PKA stimulation (fold-increase of activity) was further potentiated by *Akap11* deficiency (Fig. 7e). Conversely to D2 receptors, dopamine acting on D1-type receptors stimulates cAMP synthesis and activates PKA[91,103]. Accordingly, administration of D1 antagonists decreased PKA activity (Fig. 7f). If PKA activity is normalized to the pre-drug baseline level in a replotted figure (Fig. 7g), we observed that PKA inhibition caused by D1R antagonism was more pronounced in *Akap11*$^{-/-}$ mice. Thus loss of *Akap11* results in markedly higher basal PKA activity; however, this increased basal activity does not occlude further activation or block inhibition of PKA by dopamine receptor drugs, but rather expands the dynamic range of PKA activation.

Dopamine in the striatum regulates multiple aspects of behavior and cognition, including, but not limited to, motor control, reward processing and mood[104]. Dopamine levels induced by amphetamine are elevated in the striatum of schizophrenic patients[105]. We tested locomotor response to subcutaneous amphetamine administration, which depends on dopamine and is often used as a behavioral model of psychosis in rodents. activity (Fig. 7h,i). Wild-type mice, as expected, showed hyperactivity following amphetamine (measured by distance traveled) Initially, during the first 30 minutes after administration, *Akap11*$^{-/-}$ mice displayed less amphetamine-induced hyperactivity (AIH) than WT littermates. However, *Akap11*$^{-/-}$ mice showed a much more sustained hyperactivity response, such that at 60-90 minutes after amphetamine administration, *Akap11*$^{-/-}$ mice still showed high levels of AIH, when WT animals had returned to

baseline (Fig. 7h). Together, these pharmacological manipulations, in conjunction with imaging and behavioral readouts, suggest that dopaminergic signals are distorted by elevated PKA activity in *Akap11* mutants, resulting in prolonged AIH (a behavioral model of psychosis).

To assess whether *Akap11* mice normally display other behavioral differences (e.g. in the absence of pharmacological manipulation), we measured the rest-activity patterns of *Akap11* mutant mice continuously in their home cages from 4 weeks to 16 weeks of age using an automated homecage activity monitoring system[106] (Extended Data Fig. 7d-f). *Akap11*$^{-/-}$ mice displayed less activity than wild-types during their night-time (active) and daytime (resting) periods (Extended Data Fig. 7d). Decreased activity in *Akap11* mutants was apparent at 4 weeks of age (at the beginning of the monitoring) and remained until 12 weeks (Extended Data Fig. 7d,e). At ~8 weeks of age, *Akap11*$^{-/-}$ mice showed more activity in the period following the lights-on transition, when wild-type mice mostly fell asleep (Extended Data Fig. 7d). When we introduced a running wheel for 1 week during the assay, *Akap11*$^{-/-}$ mutant mice showed lower levels of engagement with the running wheel[107,108] (Extended Data Fig. 7g). *Akap11*$^{+/-}$ mice were intermediate in the above assays, although not statistically different from WT (Extended Data Fig. 7d-g). In the forced swim test (often used to infer “depression-like” states[109]) , *Akap11* mutant mice displayed greater immobility in a gene-dose dependent fashion (Extended Data Fig. 7h). *Akap11* mutant mice also exhibited decreased sucrose preference after the forced swim test (Extended Data Fig. 7i), an assay that can be used to measure anhedonia[110]. The behavioral deficits were not generalized - *Akap11* mutant mice were not different from WT in latency to fall in the rotarod assessment of motor coordination (Extended Data Fig. 7j), and in prepulse inhibition test (Extended Data Fig. 7k).

Figure 7

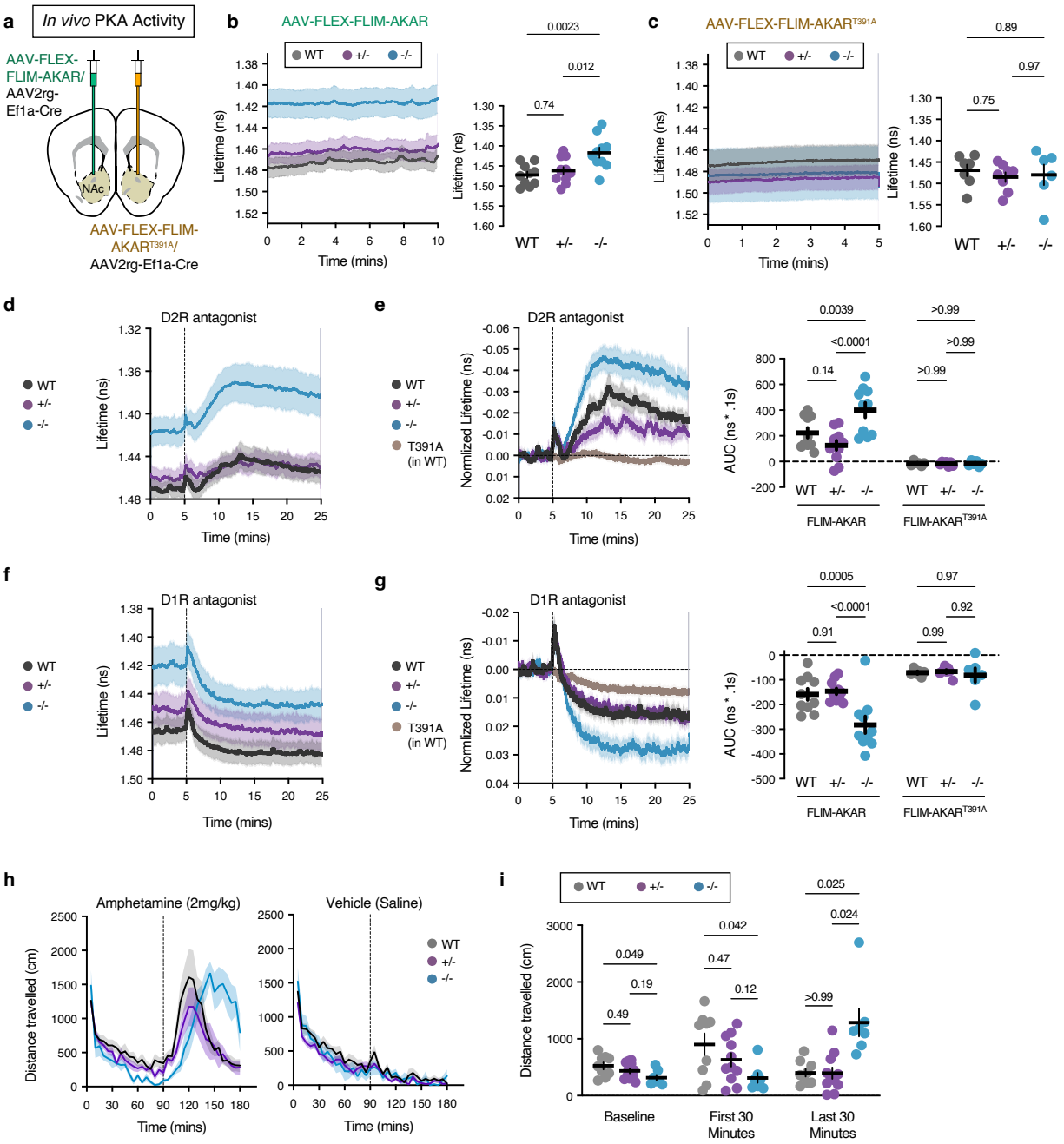

Figure 7: Fluorescence lifetime photometry (FLiP) in *Akap11* mutant mice reveals constitutively elevated PKA activity and functional alterations to striatal circuitry.

a) Schematic overview of the viral injection strategy.

b) Fluorescence lifetime of FLIM-AKAR in WT or *Akap11* mutant mice. The y-axis is inverted to reflect that decreased fluorescence lifetime corresponds to increased net PKA activity.

c) Fluorescence lifetime of FLIM-AKAR^{T391A} in WT or *Akap11* mutant mice.

d) Fluorescence lifetime changes of FLIM-AKAR in response to D2R antagonist.

e) Fluorescence lifetime changes of FLIM-AKAR in response to D2R antagonist, normalized to each genotype's baseline level of activity.

f) Fluorescence lifetime changes of FLIM-AKAR in response to D1R antagonist.
g) Fluorescence lifetime changes of FLIM-AKAR in response to D1R antagonist, normalized to each genotype's baseline level of activity.
h) Distance traveled after administration of amphetamine (2 mg/kg) or saline to WT or *Akap11* mutants.
i) Quantification of distance traveled during baseline (0-90mins), 90-120mins, and 150-180mins. Repeated measures two-way ANOVA with Tukey's post hoc test.
b-i) Data are represented as mean +/- SEM, with the shaded regions or error bars representing SEM.
b,c,e,g) Two-way ANOVA with Tukey's post hoc test.

Discussion

Genetic variation contributes substantially towards schizophrenia and bipolar disorder risk. Behavioral and psychiatric symptoms ultimately emerge from neural circuit dysfunction; however the cascade of events spanning from genetic to molecular-cellular to circuit dysfunction remain unclear. In this study, we examined *Akap11* deficiency, which was recently shown to greatly increase risk for schizophrenia and bipolar disorder. Our unbiased multi-omic profiling of mutant mice revealed two key insights about *Akap11*'s role in the brain: 1) AKAP11 is a critical regulator of PKA protein levels, resulting in a remarkable elevation of PKA activity in synapses when *Akap11* is absent. This work highlights synapse phosphorylation as an informative motif, which has been comparatively neglected in the mechanistic study of neuropsychiatric disease. 2) The striatum, the major site of dopaminergic signaling and integration in the brain, is particularly impacted by *Akap11* deficiency. Excessive or aberrant dopaminergic activity in the striatum is a long-standing hypothesis for schizophrenia pathogenesis, primarily underpinned by the antipsychotic efficacy of a specific class of dopamine receptor antagonists[102]. Through unbiased -omic studies, this study of *Akap11* mutant mice uncovers and brings attention to downstream, intracellular PKA misregulation in SPNs as an orthogonal mechanism that can disturb striatal dopaminergic signaling. Presumably, the generalized elevation of PKA activity also contributes to pathological disturbance in other brain regions, cell types and circuits, such as the PFC and thalamus, where we also saw major transcriptomic changes.

It is important to note that, in comparison with full *Akap11* knockout, the biological effects of *Akap11* heterozygosity are relatively subtle. However, many phenotypes that were readily apparent in *Akap11*$^{-/-}$, such as elevated PKA, were also seen in *Akap11*$^{+/-}$ albeit to a lesser degree– and much of this modest effect could be explained by the tempered effect of heterozygous loss of function on the levels of AKAP11 protein itself. In this context, it would be interesting to test whether or not cellular stressors, which can stimulate autophagy, could exacerbate the loss of AKAP11 protein and amplify the elevation of PKA activity in *Akap11* heterozygous mutants, thereby offering a potential way for environmental triggers to induce a disease phenotype. In any case, this nonlinear gene-dose pattern exemplifies how major effects in the homozygous condition can guide the search for latent phenotypes. To our knowledge, all previously studied large-effect SCZ risk variants[3,111,112] are also associated with intellectual disability and developmental disorders[1]. In contrast, *Akap11* has only been associated with SCZ and BP[2], making *Akap11* animal models particularly interesting to study.

Identification of genetic variants underlying SCZ and BD is accelerating at an unprecedented pace. Because these genes are diverse in nature and cellular function, the immediate or most proximal molecular abnormality would be expected to be unique to the genetic variants. Thus it is critical to identify downstream convergent cellular and circuit disturbances that are commonly impacted across these risk variants. Our findings reveal one mechanistic pathway by which a specific genetic variation leads to neural circuit dysfunction. In this case, autophagy of PKA mediated by AKAP11 is critical for maintaining normal PKA levels and kinase activity, and hence for balancing dopamine-to-PKA signaling within an appropriate dynamic range in the striatum. Our work, which started in unbiased omics fashion, highlights the fine-control of striatal dopaminergic signaling–already much implicated in psychosis pathophysiology by human and mouse model studies–as a worthy focus of future investigation. Our multi-omic analysis of the *Akap11* mouse model, together with similar investigation of other high penetrance SCZ and/or BP genes, should enable additional hypothesis-driven experiments and lead to a more nuanced understanding of the complex and heterogeneous mechanisms underlying psychiatric disease.

Supplementary materials

Extended Data Figure 1

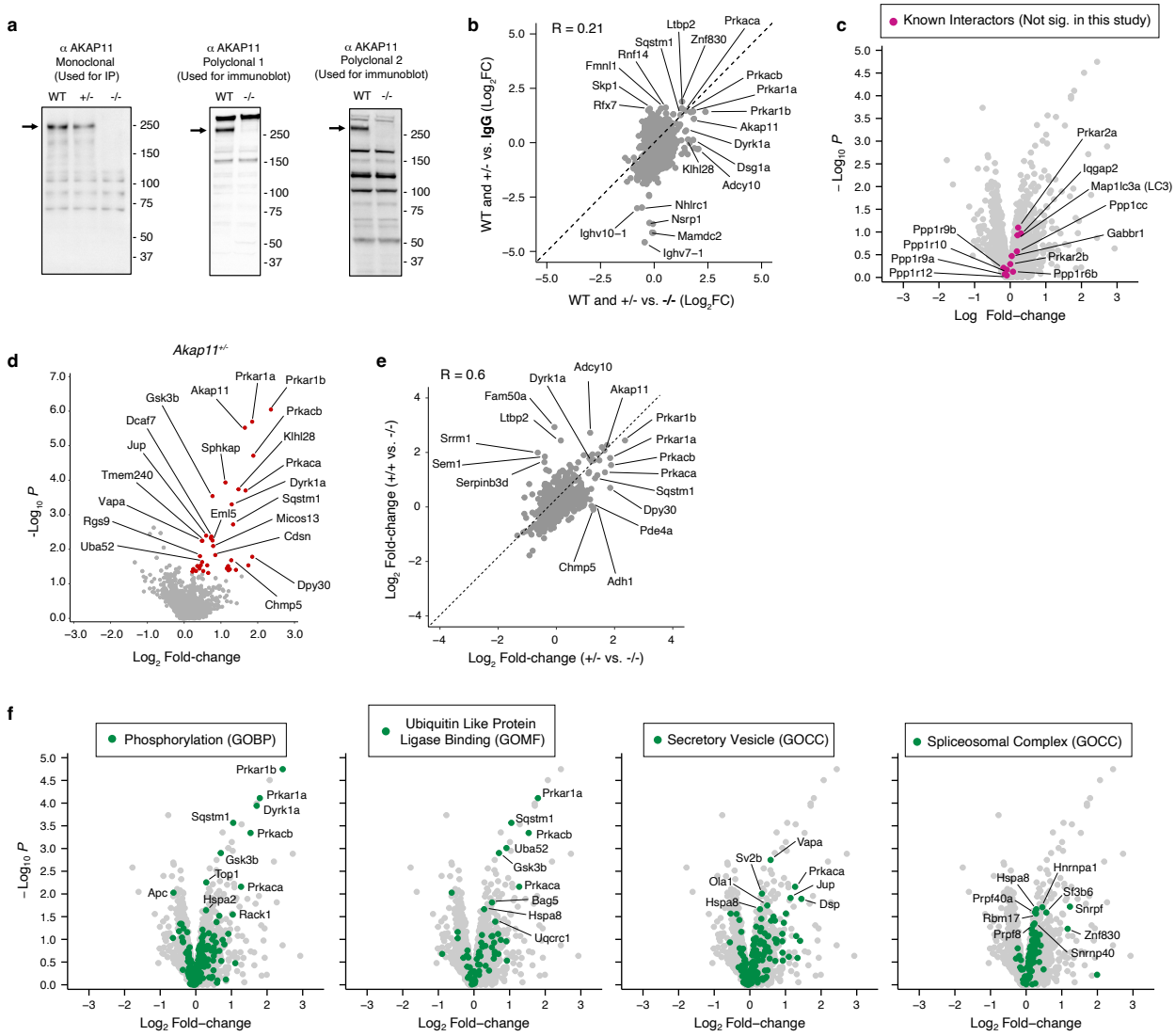

Extended Data Figure 1: AKAP11-interacting proteins and pathways in WT and in *Akap11*$^{+/-}$.
a) Immunoblots of mouse cortex using AKAP11 antibodies used in this study.
b) Log_2FC scatterplot comparing *Akap11*$^{-/-}$ vs. IgG as controls for AKAP11 IP. In these data, AKAP11 IP in WT and *Akap11*$^{+/-}$ animals were compared together against AKAP11 IP in *Akap11*$^{-/-}$ animals or IgG in WT animals.
c) Volcano plot of AKAP11 CoIP-MS (WT vs. *Akap11*$^{-/-}$). Highlighted in magenta are proteins that have been previously reported to interact with AKAP11, but were not significantly enriched in this study.
d) Volcano plot of AKAP11 coIP-MS, comparing IP in *Akap11*$^{+/-}$ vs. *Akap11*$^{-/-}$ cortex. Proteins with nominal *P* value < 0.05 and $Log_2FC > 0$, are colored red.
e) Log_2FC scatterplots comparing all proteins detected by AKAP11 IP in WT versus *Akap11*$^{+/-}$.
f) Volcano plot of AKAP11 coIP-MS. Highlighted in green are proteins within gene ontology (GO) pathways that were significantly found to be enriched by GSEA. (GOBP, Gene Ontology Biological Process; GOCC, Gene Ontology Cellular Component; GOMF, Gene Ontology Molecular Function).
b&e) R = Pearson correlation.

Extended Data Figure 2

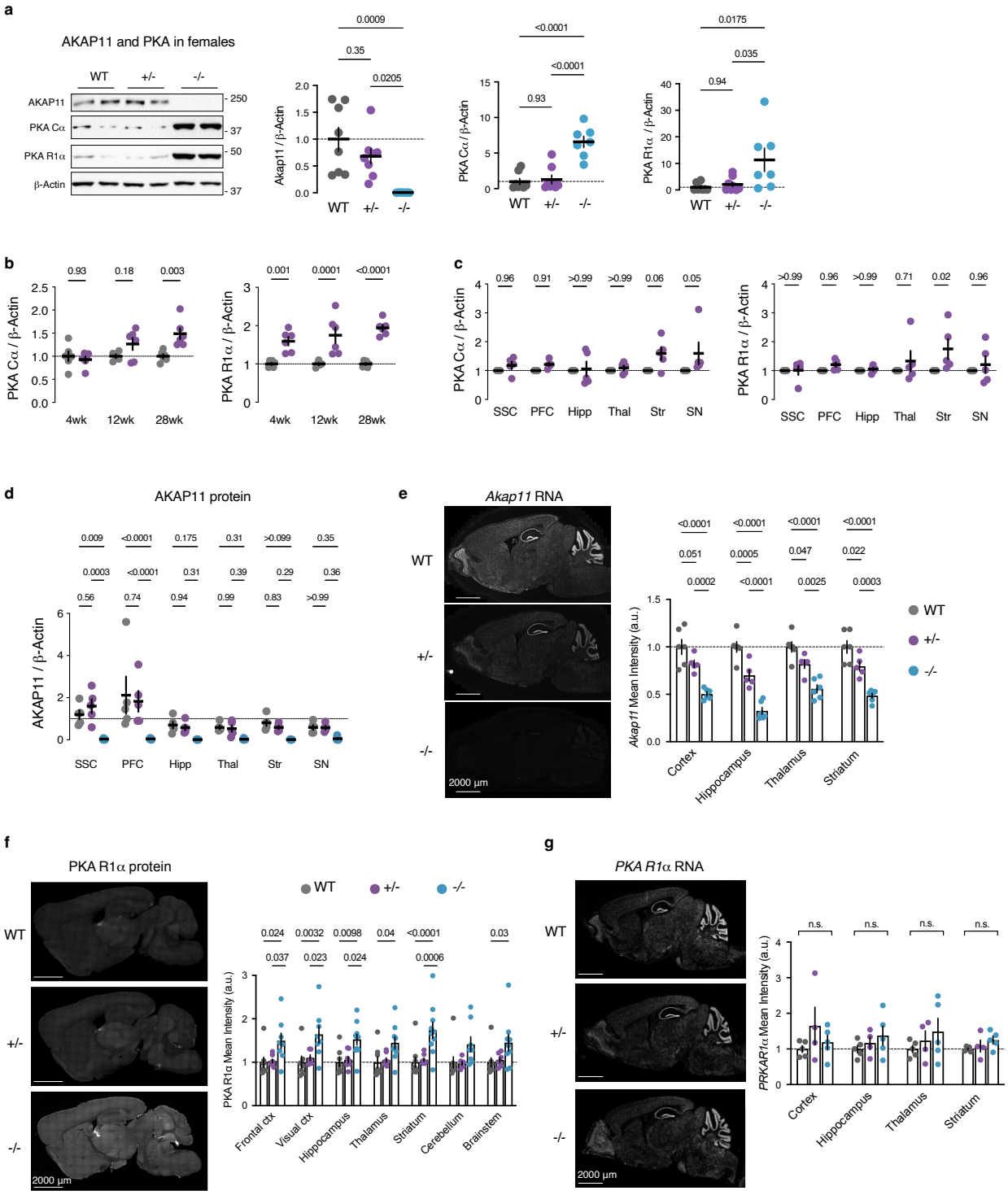

Extended Data Figure 2. PKA protein levels in *Akap11*$^{+/-}$ and *in situ*.
a) Quantifications of AKAP11 and PKA subunit protein levels in female 12wk WT and *Akap11*$^{+/-}$. One-way ANOVA with Tukey's post hoc test.
b,c) Quantifications of PKA subunit proteins levels in WT and *Akap11*$^{+/-}$. These data are also shown in Fig. 2b,c, but are rescaled here without *Akap11*$^{-/-}$ for clarity. Two-way ANOVA with Sidak's post hoc test.
d) Quantification of immunoblots from microdissected tissue from 4wk mice using antibodies against AKAP11. Representative immunoblots for these measurements are shown in Fig. 2c. *P*-values are calculated without *Akap11*$^{-/-}$ in multiple comparisons. Unlike other figures, these data are not normalized to WT within a brain region, in order to display differences in AKAP11 protein across brain regions.
e) *In situ* hybridization measurements of *Akap11* RNA. Right, quantification of mean intensity measurements within anatomical subregions. Measurements are normalized to WT controls within a region.
f) Immunofluorescence measurements of PKA R1α protein *in situ*. Right, quantification of mean PKA R1α immunofluorescence intensity measurements within anatomical subregions. Multiple comparisons adjusted *P* values < 0.05 are displayed above.
g) *In situ* hybridization measurements of *PKA R1α* RNA. Right, quantification of mean intensity measurements within anatomical subregions. Measurements are normalized to WT controls within a region.
d-g) Two-way ANOVA with Tukey's post hoc test.
a-g) Data are represented as mean +/- SEM.

Extended Data Figure 3

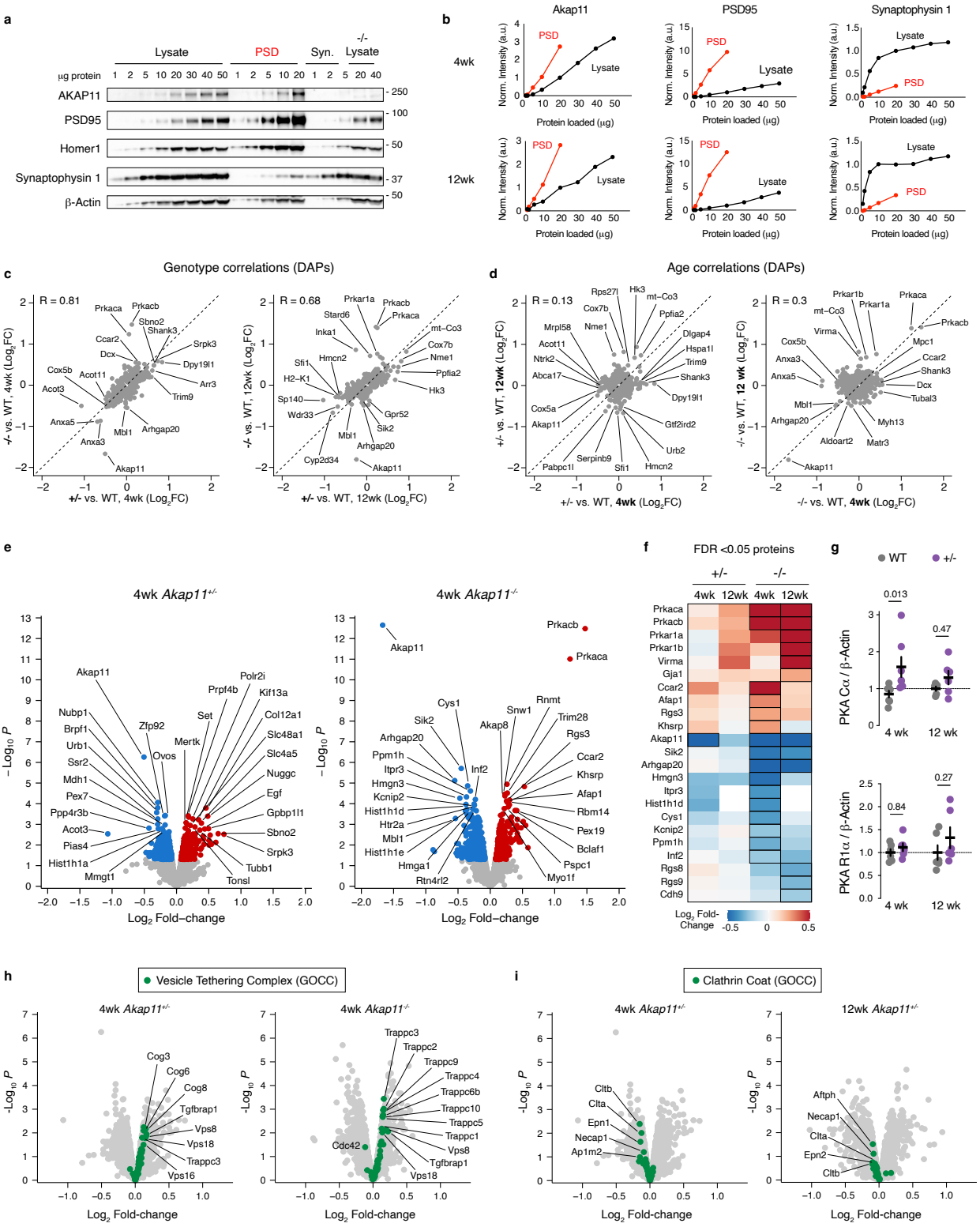

Extended Data Figure 3. Comparisons of juvenile and adult synapse proteomes.
a) Immunoblots of AKAP11 and synapse proteins across different amounts of lysate, synaptosome, and PSD-enriched fractions of 12wk cortex.
b) Quantifications of immunoblots in a). Values are normalized to 20µg lysate.
c) Log_2FC scatter plots comparing DAPs in *Akap11*$^{+/-}$ vs. *Akap11*$^{-/-}$ synapse proteomes.
d) Log_2FC scatter plots comparing DAPs in 4wk vs. 12wk synapse proteomes.
e) Volcano plots of 4 wk synapse proteomics data. Upregulated and downregulated DAPs are colored red and blue, respectively.
f) Heatmap of adjusted *P*-value (FDR) < 0.05 (black border) proteins across 4 week and 12 week synapse proteomes. Black border indicates FDR significance, including corrections for comparisons between *Akap11*$^{+/-}$ and *Akap11*$^{-/-}$.
g) Quantifications of PKA subunit proteins levels in WT and *Akap11*$^{+/-}$ synapses. These data are also shown in Fig. 3c, but are rescaled here without *Akap11*$^{-/-}$ for clarity. Data are represented as mean +/- SEM. Two-way ANOVA with Sidak's post hoc test.
h) Volcano plots of 4wk synapse proteomics data in *Akap11*$^{+/-}$. Proteins within the Vesicle Tethering Complex gene set are highlighted in green.
i) Volcano plots of synapse proteomics data in *Akap11*$^{+/-}$. Proteins within the "Clathrin Coat" gene set are highlighted in green for 4wk and 12wk animals.

Extended Data Figure 4

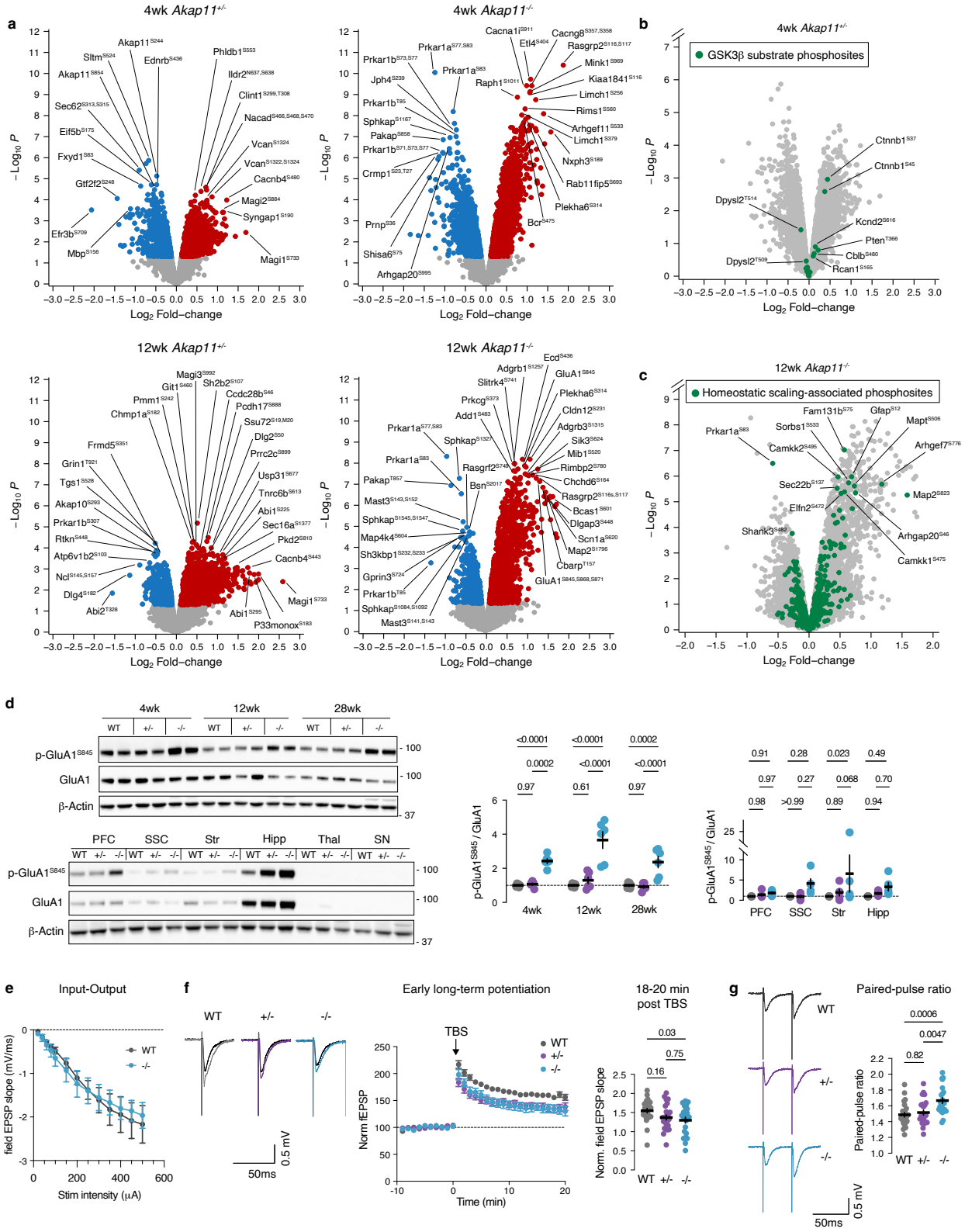

Extended Data Figure 4: Phosphoproteomic correlates of synaptic plasticity and electrophysiological characterization of synaptic strength and plasticity.

a) Volcano plots of synapse phosphoproteomics in *Akap11* mutants relative to WT. Upregulated and downregulated DAPPs are colored red and blue respectively.

b) Volcano plots of 4wk synapse phosphoproteomics for *Akap11*$^{+/-}$. Known GSK3β substrates from PhosphoSitePlus are labeled in green.

c) Volcano plots of 12wk synapse phosphoproteomics for *Akap11*$^{+/-}$. Phosphosites that are altered during scaling (24 hours of bicuculline or tetrodotoxin treatment, FDR <0.05 in Desch et al., 2021)[59] are labeled in green.

d) Immunoblotting and quantification of p-GluA1^{S845} and GluA1 in 4wk, 12wk or 28wk cortical lysate or in microdissected brain regions. Two-way ANOVA with Tukey's post hoc test.

e) Input-output (I-V) curves of field electric postsynaptic potential (EPSP) responses evoked with varying stimulation intensities (20-500uA).

f) Left, representative traces of field EPSPs before and after LTP induced by theta burst stimulation (TBS). Traces were generated by averaging the data points during the first (baseline; light lines) and last (post LTP; dark lines) two mins of the experiment. Middle, quantification of field EPSP slopes over the 30-min long early LTP experiment. Each dot represents the average field EPSP slope over 1 min. Right, quantification of field EPSP slope in minutes 18-20 following TBS.

g) Left, representative traces of paired pulse responses at 40ms stimulation intervals. Right, quantification of paired pulse ratios from *Akap11* mutants and WT brain slices.

a,c) AKAP11 phosphopeptides are omitted from *Akap11*$^{-/-}$ plots, for clarity.

d-g) Data are represented as mean +/- SEM.

f,g) One-way ANOVA with Tukey's post hoc test.

Extended Data Figure 5

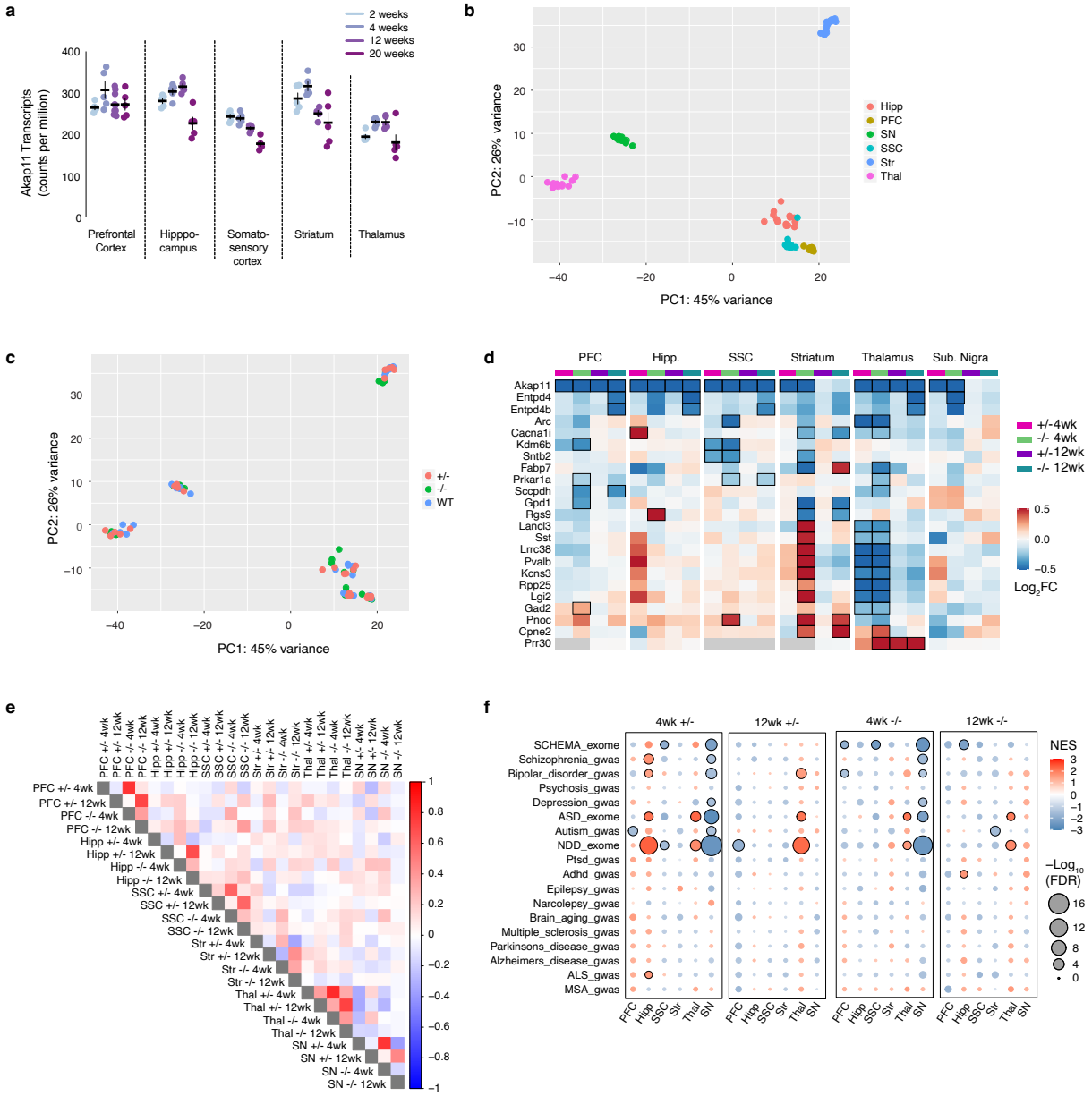

Extended Data Figure. 5: Comparisons between brain regions, ages, and genotypes in bulk RNA sequencing.
a) *Akap11* mRNA expression across brain regions and ages in wild-type mice, analyzed from data published in Farsi et al., 2023[3]. Data are represented as mean +/- SEM.
b,c) PCA plots of bulk RNA sequencing experiments, colored by a) brain region or b) genotype.
d) DEGs that reached FDR significance in at least 3 brain regions or developmental periods.
e) Log_2FC correlations between nominally significant genes ($P < 0.05$) across brain regions, ages, and genotypes.
f) GSEA results for genes associated ($P < 0.05$) with schizophrenia in exome-wide analysis[1] or in psychiatric and neurological conditions by GWAS.
d,f) Black outline indicates FDR < 0.05 significance.

Extended Data Figure 6

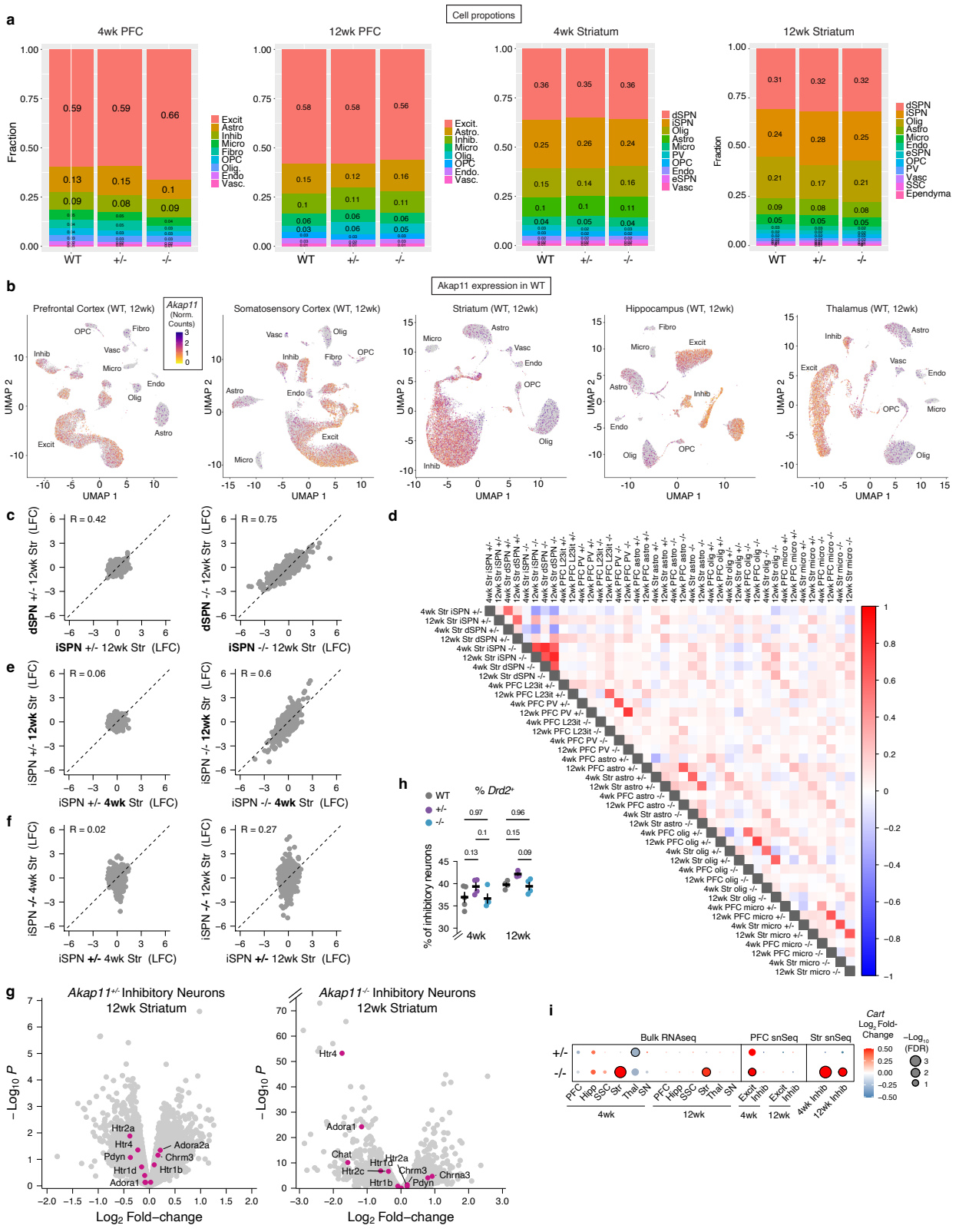

Extended Data Figure. 6: Comparisons between brain regions, age and cell types in snRNA-seq.
a) Fraction of each cell type identified across genotypes.
b) *Akap11* expression across major cell types on uniform manifold approximation and projection (UMAP) representations of cell types in different brain regions and ages of wild-type mice. This data appears in Farsi et al., 2023[3].
c) Log_2FC scatterplots comparing all genes for iSPN vs dSPN subtypes.
d) Log_2FC correlations between nominally significant genes ($P < 0.05$) across cell types.
e) Log_2FC scatterplots comparing all genes at 4wk vs. 12wk, in iSPNs.
f) Log_2FC scatterplots comparing all genes in *Akap11*$^{+/-}$ vs. *Akap11*$^{-/-}$, in iSPNs.
g) Volcano plots of transcriptomic changes identified by snRNA-seq analysis in 12wk striatal inhibitory neurons. Genes of interest related to neuromodulation and circuit development are highlighted in magenta.
h) Percentage of Drd2^{+} inhibitory neurons in the striatum. Data are represented as mean +/- SEM. Two-way ANOVA with Tukey's post hoc test.
i) Log_2FC and FDR-adjusted *P*-values for *Cart* across bulk and snRNA-seq.

Extended Data Figure 7

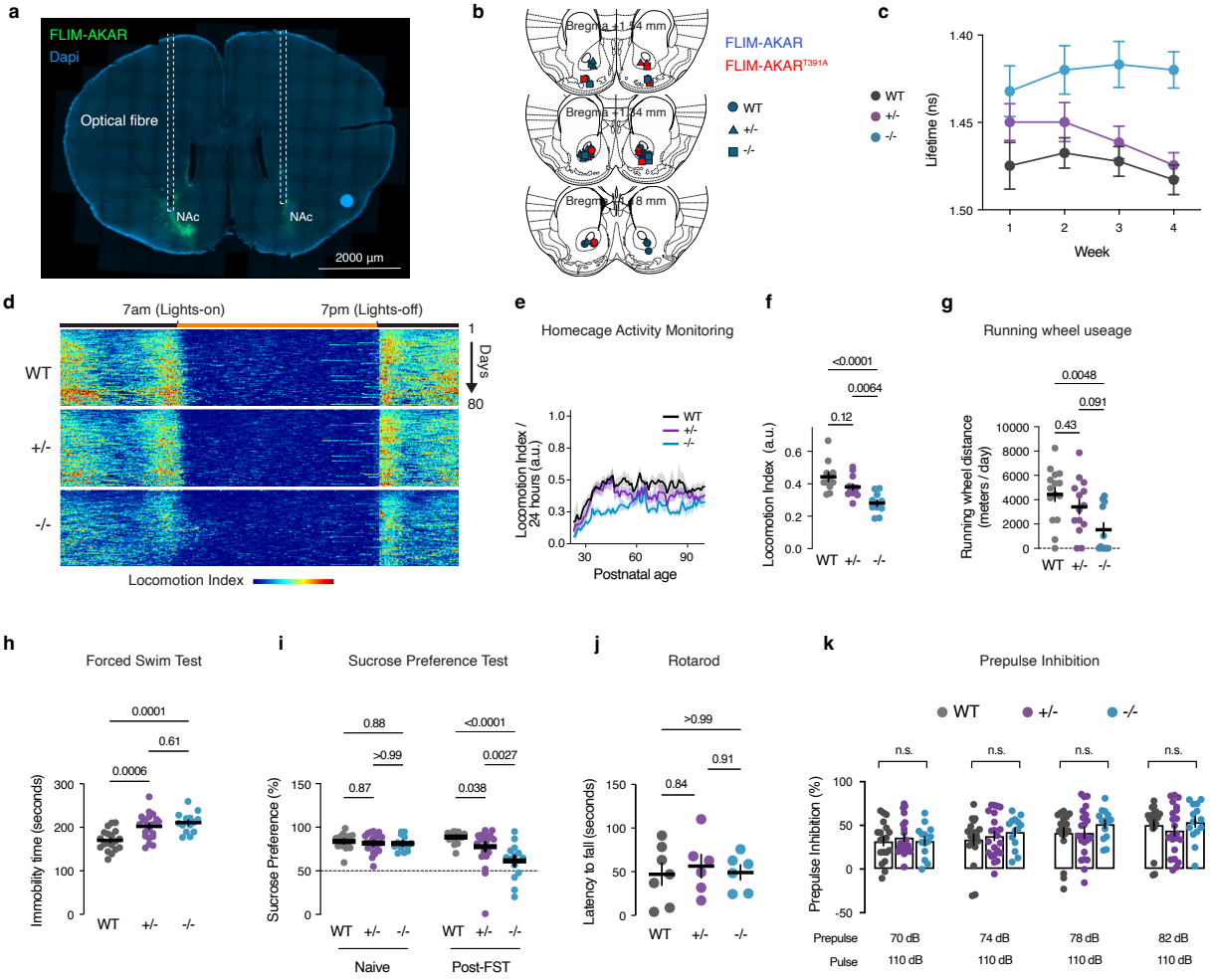

Extended Data Figure 7: Longitudinal measurement of PKA activity and behavioral tests.
a) Immunohistochemical validation of AAV injection site targeting of NAc.
b) Injection site targets of each animal in this study. Animals of different genotypes are differentiated by shape, and FLIM-AKAR variants that were injected into contralateral hemispheres are indicated by color.
c) Fluorescence lifetime of FLIM-AKAR across 4 fiber photometry recording sessions across weeks.
d) Average activity of each genotype across 24 hours in a homecage locomotor activity monitoring system. Each row is 24 hours, and 80 rows representing 80 consecutive days are shown. Yellow and black bars indicate lights-on and lights-off periods respectively.
e) Average locomotor activity across 80 days.
f) Average locomotor activity of each animal across 80 days of the assay.
g) Running wheel usage during a 1 week test period.
h) Immobility duration during the forced swim test (FST).
i) Sucrose preference of *Akap11* mutant and WT animals before and after undergoing FST.
j) Average latency to fall across 4 rotarod test trials.
k) Prepulse inhibition to an acoustic stimulus, measured as a percentage of accelerometer response to the test pulse, relative to a less intense prepulse.
c,e-k) data are represented as mean +/- SEM, with the shaded regions or error bars representing SEM.
g,h,j) One-way ANOVA with Tukey's post hoc test.
i,k) Repeated measures two-way ANOVA with Tukey's post hoc test.

Supplementary Table 1: Results of synapse proteomics and phosphoproteomics of *Akap11* mutant mice.
Supplementary Table 2: Significant pathways identified by gene set enrichment analysis of synapse proteomes of *Akap11* mutant mice.
Supplementary Table 3: Nominally significant genes from bulk RNA sequencing of *Akap11* mutant mice.
Supplementary Table 4: Significant pathways identified by gene set enrichment analysis of bulk RNA sequencing of *Akap11* mutant mice.
Supplementary Table 5: Nominally significant genes from single nucleus RNA sequencing of *Akap11* mutant mice.
Supplementary Table 6: Significant pathways from gene set enrichment analysis of bulk RNA sequencing of *Akap11* mutant mice.

Acknowledgements
We thank Kris Dickson and members of the Sheng and Granger Labs for valuable input; Ben Neale, Tarjinder Singh and Calwing Liao for consultations on human genetic evidence; Kira Brenner and Jacalyn Fahey for assistance with immunohistochemistry; Miriam Kpoyto for help with amphetamine-induced hyperlocomotion experiments; Abe Eafa and the Nate Hodgson for help with behavioral assays; Michael Dolan and Chuck Vanderburg for guidance on transcriptome experiments; Michael Sherman for packaging AAVs; Tyler Caron and Matthew Beck for help with mouse colony management and *in vivo* experiment logistics; the Broad Institute Genomic Platform for assistance with RNA sequencing. We thank the IDDRC Animal Behavior and Physiology Core, funded by NIH/NICHD P50 HD105351

Author contributions
B.J.S. and M.S. conceived and designed the -omics, biochemical, and behavioral experiments**.** Y.G., M.S. and A.G. conceived and designed fiber photometry, electrophysiology, pharmacological and behavioral experiments. B.J.S. and M.S. wrote the manuscript, with help from Y.G and A.G. and input from all authors. B.J.S. and Y.G. performed the majority of experiments and analyses in this paper. Specifically, B.J.S. performed immunoprecipitations, immunoblots, immunohistochemistry, synapse purifications, nuclei isolation, RNAseq, homecage activity measurements and analyzed these data. Y.G. performed FLiP measurements, slice electrophysiology, dopamine receptor pharmacology, amphetamine-induced hyperlocomotion and analyzed these data. A.N. processed the transcriptome data, including quality control, reference genome alignment, cell type clustering, annotation and differential expression analysis, with guidance from S.K.S., K.P.M. and supervision from J.L. M.J.K. performed nuclei isolation and library preparation for 12 week striatum and PFC snSeq datasets. B.L. designed the FLiP recording set up, calibrated the measurements and developed the analysis pipeline with guidance from B.L.S. K.B. performed LC-MS/MS for synapse proteomics and synapse phosphoproteomics and A.V.T. performed LC-MS/MS for immunoprecipitations with guidance from H.K. and S.C and analysis help from D.R.M. J.A. and C.G. helped with immunoblots. S.N. performed smFISH. I.P. and N.S. assisted with brain tissue collection and immunohistochemistry, and N.S. additionally designed and performed rotarod

behavioral tests. H.P. and N.M.N. assisted with nuclei isolation and snSeq library preparation with supervision from E.Z.M. E.Z.M. designed the snSeq protocol and guided snSeq analysis. S.A., Z.F. and X.L. helped with data analysis. N.M. conducted phosphoproteomics motif analysis with supervision from B.S. B.D. purified synapse fractions for proteomics/phosphoproteomics and provided guidance and supervision for biochemical experiments. M.S. and A.G. supervised the project and acquired funding. This work was supported by the Stanley Center for Psychiatric Research and the Harvard Brain Science Initiative Bipolar Disorder Seed Grant.

Competing Interests

M.S. is cofounder and scientific advisory board (SAB) member of Neumora Therapeutics and serves on the SAB of Biogen, Proximity Therapeutics and Illimis Therapeutics. S.A.C. is a member of the SAB of Kymera, PTM BioLabs, Seer, and PrognomIQ. B.S. serves on the Scientific Advisory Board of Annexon Biosciences and is a minor shareholder of Annexon. B.D. is a full-time employee of Vigil Neuroscience. E.Z.M. is an academic founder of Curio Bioscience.

Methods

Animals

All experiments were approved by the Broad Institute IACUC (Institutional Animal Care and Use Committee) and conducted in accordance with the NIH Guide for the Care and Use of Laboratory Animals. Heterozygous *Akap11* mice (B6.Cg-Akap11[tm1.2Jsco/J]) were obtained from The Jackson Laboratory following cryorecovery (strain #028922). As previously described[17], these mice have deletions of exons 6 and 7 of the mouse *Akap11* gene to create a knockout allele. *Akap11* mutant mice were deposited by the donor lab after 6 generations of backcrossing to the C57BL/6J background. We confirmed the genetic background of the animals to be greater than 90% C57BL/6J through SNP analysis (MiniMuga panel, Transnetyx). To establish the colony, founders were crossed to WT C57/BL6J mice (Jackson Laboratory, #000664) for one generation. Subsequently, heterozygous mice were crossed with each other to produce wild-type (WT, +/+), heterozygous (Het, +/-) and knockout (KO, -/-) littermates used for experiments. Mice were housed at AAALAC-approved facilities on a 12-hour light/dark cycle, with food and water available ad libitum. For fluorescence lifetime photometry experiments (FLiP), mice were housed in a 12h/12h light/dark reverse cycle. FLiP and pharmacological experiments were conducted in compliance with protocols approved by the Harvard Standing Committee on Animal Care, adhering to guidelines outlined in the US National Institutes of Health Guide for the Care and Use of Laboratory Animals.

Anti-AKAP11 antibodies

Two custom polyclonal rabbit anti-AKAP11 antibodies were generated for this paper and used for immunoblot experiments. For both polyclonal antibodies, the first 284 amino acids of the mouse AKAP11 protein (Uniprot reference E9Q777) were injected into rabbits, and affinity purified by a company (Genscript). The antigen sequence used was:
MAAFQPLRSSHLKSKASVRKSFSEDVFRSVKSLLQSEKELCSVSGGECLNQDEHPQLTEVTFL

GFNEETDAAHIQDLAAVSLELPDLLNSLHFCSLSENEIICMKDTSKSSNVSSSPLNQSHHSGML CVMRVSPTLPGLRIDFIFSLLSKYAAGIRHTLDMHAHPQHHLETTDEDDDDTNQSVSSIEDDFVT AFEQLEEEENAKLYNDEINIATLRSRCDAASQTTSGHHLESHDLKVLVSYGSPKSLAKPSPSVN VLGRKEAASVKTSVTTSVSEPWTQRSLY. For immunoprecipitations, we used a commercial rabbit monoclonal antibody targeting residues surrounding Alanine 1125 of mouse AKAP11 (Cell Signaling Technologies (CST), #77313). All other AKAP11 antibodies we tested, including our own polyclonal antibodies, immunoprecipitated PKA subunits in *Akap11*$^{-/-}$ brains, indicating insufficient specificity (data not shown but available upon request).

Immunoprecipitation

Twelve week-old (P120) male mice were euthanized using CO_2 inhalation, harvested around the lights-off period (Zeitgeber Time 12, ZT12) when mice are active, which was approximately ZT10-ZT14. For coIP-MS, 5 WT, 5, *Akap11*$^{+/-}$, and 5 *Akap11*$^{-/-}$ animals underwent immunoprecipitation with the AKAP11 antibody. Three WT animals underwent immunoprecipitation with IgG control. After sacrifice, cortical hemispheres were rapidly dissected and mechanically homogenized with 12 slow strokes by a Teflon homogenizer and a glass vessel in ice-cold phosphate buffered saline (PBS) with 1% Triton-X with protease (Sigma 4693159001) and phosphatase (Sigma 4906837001) inhibitors. The homogenate was centrifuged at 10,000 g (4°C) for 10 minutes and the resultant supernatant was used for immunoprecipitation. Protein concentration was measured with bicinchoninic acid assay BCA (Thermo Fisher Scientific A53225) and samples were normalized to equal protein concentrations and volumes with homogenization buffer in protein LoBind tubes (Eppendorf #022431102). For coIP-mass spectrometry, samples had 4mg of protein in a volume of 2mL. For coIP-immunoblot, samples had either 500µg or 1mg (which were matched between experimental and control samples), normalized to 1 mg/mL. Lysates were incubated overnight rotating at 4°C with 1µg anti-AKAP11 monoclonal antibody (1:20; CST 77313) or 1µg mAb IgG control (CST 3900) for mass spectrometry experiments. For coIP-immunoblot, lysates were incubated with the following primary antibodies: 1:50 Rabbit anti-AKAP11 (CST 77313), 1:50 Rabbit anti-GluA1 (CST 13185), 1:50 Rabbit anti-PKA Cα (CST 4782), 1:50 Rabbit anti-PKA R1α (CST 5675), 1:50 Rabbit anti-PKA R2β (Sigma ABS14), 1:50 Rabbit anti-VAPA (Proteintech 15275-1-AP), 1:50 Rabbit anti-VAPB (Proteintech 14477-1-AP), 1:50 Rabbit anti-GSK3α (CST 4337), 1:50 Rabbit anti-GSK3β (CST 12456), 1:50 Mouse anti-DYRK1A (Abnova H00001859-M01), 1:50 Mouse anti-P62 (Abcam ab56416). As additional negative controls, Rabbit mAb IgG (CST 3900), Normal Rabbit IgG (CST 2729) or Mouse mAb IgG2a Isotype Control (CST 61656) were diluted according to manufacturer's instructions and added in lieu of primary antibodies.

The next day, lysate-antibody mixtures were incubated with Dynabead Protein G (Invitrogen 1004D) for 1 hour at room temperature (RT), following the manufacturer's specifications. Beads were then washed three times for 10 min with PBS containing 0.02% Tween20. For coIP-immunoblotting, proteins were eluted from magnetic beads with 1x Laemmli buffer and beta-mercaptoethanol (BME) mixture (Boston biosciences BP111R, Biorad 1610737, Sigma) and boiled at 98°C for 8 min and subsequently examined by SDS-PAGE (immunoblot). For coIP-MS, samples were washed twice with ice cold 50mM Tris-HCl pH 7.5 and transferred to a new tube.

Subsequently samples were resuspended in 50µl ice cold Tris-HCl pH 7.5.

CoIP sample preparation for Liquid Chromatography-Mass Spectrometry/Mass Spectrometry (LC-MS/MS) analysis

Samples were incubated in 80 µl of urea-based digestion buffer (30 mM Tris-HCl pH=8, 0.4 µg trypsin, 1mM dithiothreitol, 2 M Urea) at 25℃ and 1000 rpm for 1h. The supernatant was then collected, followed by a second incubation in 80 µl of the same urea-based buffer at 25℃ and 1000 rpm for 30 min. The second supernatant was also collected. The beads were washed with 60 µL of wash buffer (2M Urea, 50mM Tris-HCl pH=8 wash buffer) two times, collecting both washes. The on-bead digests (supernatants) and two washes were combined into 280 µl per sample and reduced with 2.3 µl of 500mM dithiothreitol (DTT) for 30 min at 1000 rpm at 25℃. This was followed by alkylation with 4.6 µl of 500 mM iodoacetamide (IAA) for 45 min at 1000 rpm at 25℃. The samples were digested overnight with 0.5 µg of Trypsin at 700 rpm at 25℃. Reactions were quenched with formic acid (FA) at a final concentration of 1%, then desalted using reverse-phase C-18 StageTips as previously described[36] and dried down. The peptides were reconstituted in 80 µl 50mM HEPES, followed by 8 µl of neat acetonitrile (MeCN), and isobarically labeled using 500 µg of Tandem Mass Tag 18-plex (TMT18) reagent (Thermo Fisher Scientific A44520 & A52046) for 1h at 1000 rpm and 25℃. After confirming successful labeling (> 95% label incorporation), the reactions were quenched with 4 µl of 5% hydroxylamine. Samples were mixed and dried. The sample was resuspended in 300 µl of 0.1% formic acid to proceed with fractionation by bRP fractionation strategy on StageTips. The tips were packed with 3 plugs of Empore Extraction Disks SDB-RPS 47mm material. StageTips were sequentially conditioned with 100 µl of methanol (MeOH) and 100 µl of 50%MeCN/0.1%FA. The sample was loaded onto the StageTips, and washed twice with 100 µl of 0.1% FA. 25 µl of 20 mM ammonium formate was added to the stage tip for buffer exchange. It was then eluted into 8 consecutive fractions with increased organic content at 100 µl per elution step (5, 10, 15, 20, 23, 27, 30 and 45% MeCN in 20 mM ammonium formate). The fractions were transferred to HPLC vials and dried.

LC-MS/MS analysis of coIP samples

The samples were analyzed on a Q Exactive HF-X mass spectrometer with a Vanquish Neo UHPLC system (Thermo Fisher Scientific). The solvents used for the HPLC system were solvent A (0.1% FA) and solvent B (0.1% FA/100% MeCN). The samples were injected into a 75-µm ID PicoFrit column packed manually to approximately 28 cm of length with ReproSil-Pur C18-AQ 1.9-µn beads (Dr. Maisch) and heated to 50℃ for chromatographic separation.
The bRP fractions were loaded into the column at a flow rate of 200nL/min. The chromatography consists of a 110-min method with a gradient of 1.6–5.4% solvent B for 1 min, 18–27% B for 22 min, 27–54% B for 9 min, 54–72% B for 1 min, followed by a hold at 72% B for 5 min and 72%-45% B for 10 min. The mass spectrometer was operated in data-dependent acquisition mode. The MS parameters were set as follows: MS1, r=60,000; MS2, r=15,000; MS1 AGC target of 3e6 with maximum injection time of 10ms; MS2 for the 20 most abundant ions using an AGC target of 5e4 and maximum injection time of 105ms; and normalized collision energy of 28.

Data analysis of the coIP-LC-MS/MS experiment

Collected data were analyzed using the Spectrum Mill software package (Broad Institute). All extracted spectra were searched against a UniProt database containing mouse reference proteome sequences retrieved on 04/07/2021 and containing 55734 entrees. Fixed modifications were carbamidomethylation at cysteine. TMT labeling was required at lysine, but peptide N termini could be labeled or unlabeled. Allowed variable modifications were protein N-terminal acetylation and oxidized methionine.

Protein quantification was achieved by taking the ratio of TMT reporter ions for each sample over the median of all channels. TMT18 reporter ion intensities were corrected for isotopic impurities in the Spectrum Mill protein/peptide summary module using the afRICA correction method which implements determinant calculations according to Cramer's Rule79 and correction factors obtained from the reagent manufacturer's certificate of analysis for lot numbers XD343709 and XD346675. After performing median-MAD normalization, a moderated two-sample t-test was applied to the datasets to compare WT, *Akap11*$^{+/-}$ and *Akap11*$^{-/-}$ sample groups.

Immunoblot

Four week (P30) or 12 week (P120) male mice were euthanized using CO_2 inhalation between ZT10-ZT14, after which whole cortices were rapidly dissected and flash-frozen in liquid nitrogen. Single hemispheres were homogenized in a 5 ml ice-cold homogenization buffer (1% SDS in PBS) supplemented with phosphatase (Sigma 4906837001) and protease inhibitors (Sigma 4693159001), using the mechanical homogenization procedure described above. After BCA (Thermo Fisher Scientific, A53225 or 23225) quantification of protein concentration, samples were diluted with 6X Laemmli buffer with BME (Boston Bioproducts, BP-111R) or 2x Laemmli buffer (Biorad, 1610737) with BME (Sigma, M3148) to a final concentration of 1x and boiled in reducing SDS loading buffer at 98°C for 8 min. After preparation, sample aliquots were frozen at -80°C. Before running on a gel, samples were thawed, heated at 98°C for 1 min and centrifuged briefly. Samples were run on NuPAGE 3-8% Tris Acetate gradient gels (Invitrogen) at a constant voltage. Equal amounts of sample were loaded unless otherwise specified (Extended Data Figs. 3a,b). For Fig. 2a, a subset of smaller molecular weight proteins were tested on 4-20% tris glycine gradient gels (Invitrogen). Proteins were transferred to 0.2 mm nitrocellulose membranes using semi-dry transfer (Bio-Rad Transblot Turbo; 25V 30 min) and visualized by Coomassie stain (Sigma, P7170). Subsequently, membranes were blocked with 5% milk in Tris-buffered saline with 0.2% Tween 20 (TBST). Membranes were incubated overnight with primary antibodies in 5% milk TBST with gentle rotation at 4°C. Membranes were incubated with primary antibodies overnight at 4°C, washed three times with TBST for 10 min, and then incubated with secondary HRP-conjugated antibodies raised against the appropriate species for 1 hour at RT. After 3 additional TBST washes, membranes were imaged on ChemiDoc MP (Bio-Rad) and analyzed using Image Lab Software (Bio-Rad). Enhanced chemiluminescence (Thermo, 34580 and 34096) and exposures were optimized to obtain signals in the linear range. Membranes were then stripped (Thermo, 46430),washed three times, re-blocked with 5% milk in TBST, and re-probed as described above. For cortical lysate immunoblots, 20µg of protein was loaded. For microdissected brain regions, 15 or 20 µg or protein and 5 or 10 µg synapse fraction protein

were used for SDS-PAGE, unless otherwise specified (Extended Data Fig. 3a,b). For all experiments, protein loading amounts were consistent across samples.

For coIP-immunoblot, the following antibodies were used during SDS-page (after immunoprecipitation): 1:1000 Mouse anti-PKA R1α (BD 610609), 1:1000 Mouse anti-PKA Cα (BD 610980), 1:1000 Mouse anti-PKA R2β (BD 610625), 1:1000 Mouse anti-GluA1 (NeuroMab 75-327), 1:1000 Rabbit anti-Vinculin (CST 4650), 1:1000 Rabbit anti-VAPA (Proteintech 15275-1-AP), 1:1000 Rabbit anti-VAPB (Proteintech 14477-1-AP), 1:1000 Rabbit anti-GSK3α (CST 4337), 1:1000 Rabbit anti-GSK3β (CST 9315), Mouse anti-GSK3α/β (Thermo Fisher Scientific 44-610) ,1:1000 Rabbit anti-Dyrk1a (CST 2771), 1:1000 Rabbit anti-P62 (CST 5114). For coIP-immunoblot, we used horseradish peroxidase (HRP)-conjugated secondaries recognizing the host species of the primary antibody (Thermo Fisher Scientific 31460 and 31430 for rabbit and mouse respectively). When the IP and immunoblot antibodies were from the same species (Fig. 1g), we used secondaries that are selective towards non-denatured IgG (1:1000, TrueBlot HRP, Rockland, 18-8816-33 and 18-8817-30).

For immunoblot, the following antibodies were used:
1:1000 Rabbit anti-AKAP11 (Custom R171), 1:1000 Rabbit anti-AKAP11 (Custom R173), 1:1000 Mouse anti-PKA R1α (Thermo Fisher Scientific MA5-24981), 1:1000 Rabbit anti-PKA R1α (CST 5675), 1:1000 Rabbit anti-PKA Cα (CST 4782), 1:1000 Rabbit anti-Iqgap1 (Abcam ab86064), 1:1000 Rabbit anti-Dyrk1a (CST 2771), 1:1000 Rabbit anti-GSK3α (CST 4818), 1:1000 Rabbit anti-GSK3β (CST 9315), 1:1000 Mouse anti-P62 (Abcam ab56416), 1:1000 Rabbit anti-LC3A/B (CST 12741), 1:1000 Rabbit anti-VAPA (Proteintech 15275-1-AP), 1:1000 Rabbit anti-β Catenin (CST 8480), 1:1000 Mouse anti-Protein Phosphatase 1 (Santa Cruz SC-7482), 1:1000 Rabbit anti-Sik2 (CST 6919), 1:1000 Rabbit anti-p-GSK3α^{S21} / anti-p-GSK3β^{S9} (CST 8566), 1:1000 Rabbit anti-p-GSK3α / anti-p-GSK3β (CST 5676), 1:1000 Rabbit anti- p-GSK3β^{S9} (CST 9336), 1:1000 Rabbit anti- p-GluA1^{S845} (CST 8084), 1:1000 Rabbit anti- GluA1 (CST 13185), 1:1000 Mouse anti- GluA1 (NeuroMab 75-327), 1:1000 Mouse anti-PSD95 (BioLegend 810301), 1:1000 Rabbit anti-Homer1 (Synaptic Systems 160003), 1:1000 Guinea Pig anti-Synaptophysin 1(Synaptic Systems 101004). 1:1000 Mouse anti-PSD95 (clone K28/43, Antibodies Inc 75-028). HRP-conjugated anti-Rabbit or anti-Mouse IgG (Thermo Fisher Scientific 31460 and 31430). β-actin was probed using an HRP conjugated primary antibody after all other proteins were probed (1:10,000. Thermo Fisher Scientific A3854). Otherwise, we used HRP conjugated secondaries recognizing the host species of the primary antibody (Thermo Fisher Scientific 31460 and 31430 for rabbit and mouse respectively).

Synapse purifications

Synapse fractions were purified as we described previously[36,113,114]. Flash-frozen whole cortex and subcortical basal forebrain was mechanically homogenized with 12 slow strokes by a Teflon homogenizer and glass vessel in ice-cold homogenization buffer (5 mM HEPES pH 7.4, 1 mM $MgCl_2$, 0.5 mM $CaCl_2$, supplemented with phosphatase (Sigma 4906837001) and protease inhibitors (Sigma 4693159001). The homogenate was centrifuged for 10 min at 1,400 g (4°C) and the resulting supernatant (S1) was re-centrifuged at 13,800 g for 10 min (4°C). The resulting pellet (P2) was resuspended in 0.32 M Sucrose, 6 mM Tris-HCl (pH 7.5) and layered

gently on a 0.85 M, 1 M, 1.2 M discontinuous sucrose gradient (all layers in 6 mM Tris-HCl pH 7.5) and ultracentrifuged at 82,500 g for 2 hours (4°C). For synapse mass spectrometry experiments, phosphatase inhibitors were added to 1 M and 1.2 M sucrose buffers. The synaptosome fraction, which sediments at the interface between 1 M and 1.2 M sucrose, was collected. An equal volume of ice-cold 1% Triton X-100 (in 6 mM Tris-HCl pH 7.5) was added, mixed thoroughly, and incubated on ice for 15 min. The mixture was ultracentrifuged at 32,800 g for 20 min (4°C), and the pellet (the synapse fraction) was collected by resuspension in 1% SDS. A small aliquot was taken to measure the protein concentration using the Pierce Micro BCA assay (ThermoFisher Scientific, 23235) or BCA (ThermoFisher Scientific A53225) and the remaining protein was stored at -80°C until processed for MS or immunoblot. For synapse proteomics, sixteen synaptic fractions extracted from the cortex of wild type, *Akap11*$^{+/-}$ and *Akap11*$^{-/-}$ mouse brains were used for the proteomics study using tandem mass tag (TMT) isobaric labeling strategy for quantitation. At 4 weeks, sample sizes were n= 5 WT, 5 *Akap11*$^{+/-}$ and 6 *Akap11*$^{-/-}$. At 12 weeks, the sample sizes were n= 6 WT, 5 *Akap11*$^{+/-}$ and 5 *Akap11*$^{-/-}$.

Processing of samples for proteomics and phosphoproteomics

Synapse fractions from animals at 4 weeks and 12 weeks were processed in two separate TMT16 plexes as described before [36]. Briefly, all samples were prepared in a 1% SDS buffer and digested using S-Trap™ sample processing technology (Protifi) following manufacturers recommendations. Following digestion, 100 µg of each sample was reconstituted in 20µl of 50mM HEPES and labeled with 200 µg TMT16 reagent (Thermo Fisher Scientific A44520). After verifying successful labeling of more than 95% label incorporation reactions were quenched, mixed, desalted and dried down. TMT16 labeled peptides were fractionated by high pH reversed-phase chromatography on a 4.6 mm x 250 mm Zorbax 300 extend-c18 column (Agilent). One-min fractions were collected during the entire elution and fractions were concatenated into 18 proteome fractions for LC-MS/MS analysis. Five percent of each fraction was removed for proteome analysis. The remaining of each of the 18 fractions were further concatenated to 9 fractions and dried down for phosphopeptide enrichment using immobilized metal affinity chromatography (IMAC).

LC-MS/MS analysis for synapse fractions

One microgram of each proteome fraction and half of each of the IMAC fractions were analyzed on a QE-HFX mass spectrometer (Thermo Fisher Scientific) coupled to an Easy-nLC 1200 LC system (Thermo Fisher Scientific). Samples were separated using 0.1% Formic acid/3% Acetonitrile as buffer A and 0.1% Formic acid /90% Acetonitrile as buffer B on a 27cm 75um ID picofrit column packed in-house with Reprosil C18-AQ 1.9 mm beads (Dr Maisch GmbH) with a 110 min gradient consisting of 2-6% B in 1 min, 6-20% B in 62 min, 20-30% B for 22 min, 30-60% B in 9 min, 60-90% B for 1 min followed by a hold at 90% B for 5 min. The MS method consisted of a full MS scan at 60,000 resolution and an AGC target of 3e6 from 350-1800 m/z followed by MS2 scans collected at 45,000 resolution with an AGC target of 3e6 from 300-1800 m/z followed by MS2 scans collected at 35,000 resolution with an AGC target of 1e5 and 5e4 for proteome and phosphoprotome fractions, respectively and a maximum injection time of 105 ms. Dynamic exclusion was set to 15 seconds. The isolation window used for MS2 acquisition was

0.7 m/z and 20 most abundant precursor ions were fragmented with a normalized collision energy (NCE) of 29 optimized for TMT16 data collection.

Database search and MS/MS quantification for PSD fractions

All the datasets were searched on Spectrum Mill MS Proteomics Software (Broad Institute) using mouse database downloaded from Uniprot.org on either 12/28/2017 or 04/07/2021 containing 47,069 or 55,734 entrees for 4 weeks and 12 weeks coIP-MS experiments, respectively[115]. Search parameters included: ESI Qexactive HCD v4 35 scoring parent and fragment mass tolerance of 20 ppm, 40% minimum matched peak intensity, trypsin allow P enzyme specificity with up to four missed cleavages, and calculate reversed database scores enabled. Fixed modifications were carbamidomethylation at cysteine. TMT labeling was required at lysine, but peptide N-termini could be labeled or unlabeled. Variable modifications were allowed for protein N-terminal acetylation and oxidized methionine as well as phosphorylated serine, threonine, and tyrosine for the phosphoproteome datasets. Protein quantification was achieved by taking the ratio of TMT reporter ions for each sample over the TMT reporter ion for the median of all channels. TMT16 reporter ion intensities were corrected for isotopic impurities in the Spectrum Mill protein/peptide summary module using the afRICA correction method which implements determinant calculations according to Cramer's Rule and correction factors obtained from the reagent manufacturer's certificate of analysis (Thermo Fisher Scientific, 90406) for lot numbers VH310017 for both synapse proteomics experiments. Median normalization was applied to both proteome and phosphoproteome datasets prior to statistical analysis. Additionally, phosphosite changes were normalized for changes in protein abundances by fitting a global linear model between the phosphosite and the cognate protein and extracting the residuals. A moderated two-sample t-test was applied to the datasets to compare WT, *Akap11*$^{+/-}$ and *Akap11*$^{-/-}$ sample groups. For proteins with multiple isoforms, the isoform with the greatest abundance (number of spectra observed) was displayed in the plot.

Annotations from Phosphosite Plus

Kinase substrate annotations were downloaded from https://www.phosphosite.org on June 20, 2022. In this database, some kinase substrate sites are inaccurately attributed to a kinase to which it is indirectly related. For example, Grin2b^{Y1472} is annotated as a PKA Cα substrate in phopshopsite.org (see Fig. 4b, but is actually a PKC substrate[116]. Similarly, Ctnnb1^{S45} is annotated as a Gsk3β substrate in phosphosite.org, but is actually a CK1 substrate[45]. These discrepancies were not adjusted for this manuscript in order to maintain unbiased usage of the database.

Phosphoproteomics motif analysis

Motif enrichment analysis was performed to generate motif logos using the pyproteome Python library[117]. Motif logo enrichment values were calculated according to the method described for pLogo[118]. Peptide 15-mers around each phosphorylation site were generated by Spectrum Mill "VMsiteFlanks". Foreground and background N-mers were extracted from protein-aligned sequences, using '-' to pad N-and C-terminal peptides. Quantification values from identical N-mers (mis-cleaved, oxidized, or multiply-phosphorylated peptides) were combined by taking the

median value. Log odds enrichment values are equal to ($-log\frac{sf(x-1)}{cdf(x)}$), with k = the count of amino acids at that relative position for phosphosites in a foreground collection ($P < 0.05$; FC > 1.25 or FC < 0.8). Survival function (sf) and cumulative distribution functions (cdf) were calculated using scipy's hypergeometric distribution model (scipy.stats.hypergeom), with: n = the total number of foreground N-mers; K = the count of amino acids at that position in the background collection; and N=the total number of background N-mers.

Immunofluorescence

15-17-week-old male mice were euthanized under isoflurane with transcardial perfusion of ~25 mL with PBS followed by ~25 ml 4% paraformaldehyde (PFA). These mice also underwent an 1 hour open field assays for a separate study [7], at 4 weeks and 12 weeks of age. Brains were post-fixed overnight in 4% PFA, and washed the next day four times with PBS for 15 min. Tissues were cryoprotected for 72 hours and stored at 4°C until sectioning. Brains were sectioned on a vibratome (Leica) at either 40 or 60µm thickness (consistent within technical replicates) and stored in a freezing buffer (0.1M PBS, 30% ethylene glycol, 30% glycerol, 0.01% sodium azide).

For immunostaining, free-floating sections were first rinsed 4x with PBS for 10 min. Sections were blocked and permeabilized with 1 hour RT incubation in a blocking solution. For the first technical replicate, we used 5% Normal Goat Serum (Sigma, NS02L), with 10% BSA + 0.2% Triton. For the second technical replicate, we used 5% Normal Donkey Serum (Jackson, 017-000-121) + 0.2% Triton in PBS for 60 min. Primary antibodies were diluted in blocking solution and incubated overnight at 4°C, rotating gently. The following day, sections were rinsed 3x for 15 min in PBS containing 0.2% Triton at RT on a shaker. DAPI (Thermo Fisher Scientific, 62248) was added to PBS at a final concentration of 1:5000 (for the first technical replicate) or 1:10,000 (for the second technical replicate) before mounting. The following primary and secondary antibodies were used: PKA Ca (CST 4782, 1:100), PKA R1a (ThermoFisher MA5-24981, 1:100). Donkey anti Rabbit 488 (Invitrogen A32790), Donkey anti-Mouse 555 (Invitrogen A32773), Goat anti Rabbit 488 (Invitrogen A11034), Goat anti-Mouse 555 (Invitrogen A32727). Whole sections were imaged with a Zeiss Axioscan 7 Slidescanner using exposure and intensity settings that were constant across samples within technical replicates.

PKA R1α was quantified in FIJI using the freehand selection tool and the intensity measurement function. Regions were selected using the Allen Brain Atlas as a reference. Experimenters were blind to conditions during analysis. For representative images, brightness levels were uniformly increased across the whole images with Zen software (Carl Zeiss) and scaled down to 10% to accommodate the large field of view of the stitched image.

Tissue collection for RNA sequencing

For bulk and snRNA-seq, mice were harvested between ZT9 and ZT15, near the animals active period at ZT12. Brain tissues for bulk and snRNA-seq were prepared as described[3], and also available at protocols.io (https://www.protocols.io/view/fresh-frozenmouse-brain-preparation-for-single-nu-bcbrism6). At 4 and 12 weeks of age, male WT, *Akap11*$^{+/-}$ and *Akap11*$^{-/-}$ mice were

anesthetized by administration of isoflurane in a gas chamber. Within each age, 4 mice per genotype were harvested for snRNA-seq, with the exception of 4 week striatum, which had 5 WT samples. For bulk RNA-seq, 5 mice per genotype within an age were collected, with the exception of the following 4 week samples: *Akap11*$^{+/-}$ SSC and WT Hipp had 6 samples and *Akap11*$^{-/-}$ str and WT PFC had 4 samples.

Transcardial perfusions were performed with ice-cold Hank's Balanced Salt Solution (HBSS, Gibco 14175-095) in mice anesthetized with 3% isoflurane delivered continuously via nose cone. Brains were then frozen gradually over liquid nitrogen vapor and stored at –80°C with tubes containing O.C.T. (optimal cutting temperature) freezing medium (Tissue-Tek) to prevent desiccation. Brain region microdissections were performed by hand in a cryostat (Leica CM3050S), with a ophthalmic microscalpel (Feather safety razor P-715) or 1.5 mm diameter biopsy punch (Integra 33-31A). PFC, Hipp and SSC were excised by hand. SN and Thal were collected by biopsy punch. For snRNA-seq studies, both dorsal and ventral striatum were collected together with a microscalpel, while for bulk RNA-seq, dorsal striatum was collected by punch. All brain regions were identified according to the Allen Brain Atlas. Dissected tissues were placed into a precooled 1.5-ml PCR tube and stored at –80°C.

<u>RNA extraction and bulk RNA-seq library preparation</u> RNA was prepared from micro-dissected tissues using RNeasy Mini Kit (Qiagen, 74106) following the manufacturer's instructions. Briefly, tissue samples were lysed and homogenized, placed into columns, and bound to the RNeasy silica membrane. Next, contaminants were washed away. Columns were treated with DNase (Qiagen) to digest residual DNA and concentrated RNA was eluted in water. RNA concentration was measured using a NanoDrop Spectrophotometer and RNA integrity (RIN) with RNA pico chips (Agilent) using a 2100 Bioanalyzer Instrument (Agilent). Purified RNA was stored at -80°C until library preparation for bulk RNA-seq analysis. Bulk RNA-seq libraries were prepared using a TruSeq Stranded mRNA Kit (Illumina) following the manufacturer's instructions. 200 ng of isolated total RNA from each sample was used and the concentration of resulting cDNA library was measured with High Sensitivity DNA chips (Agilent) using a 2100 Bioanalyzer Instrument (Agilent). A 10 nM normalized library was pooled, and sequencing was performed on a NovaSeq S2 (Illumina) with 50 bases each for reads 1 and 2 and 8 bases each for index reads 1 and 2.

For snRNA-seq library preparation, brain tissue dissection and nuclei extraction were performed within 16 hours to avoid desiccation and freeze-thaw cycles. A gentle, detergent-based dissociation was used to extract the nuclei, according to a previously published protocol [119] also available at protocols.io (https://www.protocols.io/view/frozen-tissue-nuclei-extraction-bbseinbe). Extracted nuclei were then loaded into the 10x Chromium V3.1 system (10x Genomics) and library preparation was performed according to the manufacturer's protocol. A 10 nM normalized library was pooled, and sequencing was performed on a NovaSeq S2 (Illumina) with 28 and 75 bases for reads 1 and 2, respectively, and 10 bases each for index reads 1 and 2.

Bulk RNA-seq DE analysis

Bulk RNA-seq gene and isoform expression levels were estimated using RSEM v1.3.0[120]. rsem-prepare-reference was run with default parameters to generate the M25 (GRCm38.p6) GENCODE reference. Expression values were calculated using rsem-calculate-expression with the following flags: --bowtie2, --paired-end, --estimate-rspd, --append-names, and –sort-bam-by-coordinate. DE analysis was performed using DESeq2 v1.20.0[121] for each brain region and age. Replicates of all genotypes for a given brain region and age pair were read into a single DESeq object to ensure consistent normalization across genotype comparisons. The DESeq2 lfcShrink function was used to adjust Log_2 Fold-Change (Log_2FC) values using the 'normal' shrinkage estimator. Differentially expressed genes (DEGs) were defined as genes with a Benjamini-Hochberg adjusted *P*-value less than 0.05.

Single-nucleus RNA-seq analysis

snRNA-seq reads were aligned to an mm10 mouse reference genome containing introns (https://cf.10xgenomics.com/supp/cell-exp/refdata-gex-mm10-2020-A.tar.gz) using the Cell Ranger v3.0.2 pipeline (10x Genomics)[122]. Cell Ranger count was run with default parameters and the following additional flags: --chemistry=SC3Pv3 and --expect-cells=15000. Replicates for the 4-week STR dataset were down-sampled to contain the same number of reads per cell using Cell Ranger aggr with default parameters.

Seurat v4.0.3[123] was used to analyze Unique Molecular Identifier (UMI) counts. Nuclei expressing less than 500 genes were removed and the remaining nuclei were normalized by total expression, multiplied by ten thousand, and log transformed. The data were then scaled using Seurat's ScaleData function. Seurat's RunPCA function was used to perform linear dimension reduction on the variable genes within the scaled data. Clustering in the PCA space was then run using Seurat's FindNeighbors and FindClusters functions and the clusters were visualized using Seurat's RunUMAP function. Doublet identification was performed using the Scrublet v0.2.3[124]. Python package with default parameters. Clusters and nuclei with a scrublet score above the region-specific thresholds were determined to be doublets and were removed from the data. The table below shows the used scrublet score thresholds for all snRNA-seq datasets:

Dataset	Scrublet Score Threshold
P30-PFC	0.36
P30-ST	0.2
3m-PFC	0.4
3m-ST	0.4

Cluster cell type assignment was evaluated using region-specific cell type marker genes. Neuronal subtypes were identified by re-clustering the nuclei of a given major cell type and evaluating expression of subtype-specific marker genes. Marker genes for the more widely classified major cell types and subtypes were identified in the literature[125]. Rarer cell types and

subtypes were identified using Seurat's FindMarkers function. The clusters were then identified by searching cluster-specific marker genes on mouseBrain.org[126] and or dropviz.org[127].

Pseudobulk DE analysis

snRNA-seq differential expression (DE) analysis was performed using the pseudobulk approach. For each dataset, counts were grouped by cell type and replicate, then gene counts were summed across each replicate within a cell type, resulting in one count value per replicate per cell type. Surrogate variable analysis (SVA) was conducted using the sva v3.42.0 R package[128] to account for unknown sources of variation within each experiment. Differential expression analysis was then run with the covariates identified by SVA using the EdgeR v3.22.3 R package[129]. DEGs were defined as genes with a Benjamini-Hochberg adjusted *P*-value <0.05.

Gene set enrichment analysis

GSEA was performed with the R Bioconductor package *fgsea*[130] using C5 ontology gene sets obtained from the Molecular signatures database (MSigDB) on September 28, 2022. Genes were pre-ranked using their test-statistics within each comparison, and their *Homo sapiens* homolog-associated were used for the analysis. For genes or proteins with multiple isoforms, the isoform with the largest effect-size (absolute value of the t-statistic) was used for pre-ranking. Because the enrichment analyses were carried out using the proteins' gene symbols, we use the terms gene set and protein set interchangeably in this study. For each of these gene sets, mouse gene symbols from transcriptomics and proteomics results were mapped to matching *Homo sapiens* homolog-associated gene symbols through annotations extracted from Ensembl's BioMart data service; the human symbols were then used to perform GSEA. A list of all significant GO terms (FDR < 0.05) for all datasets are provided in Supplementary Tables.

Curated gene sets

Prioritized SCZ and BD GWAS-associated common risk genes (Fig. 5f) included the 106 protein-coding "prioritized" genes from Trubetskoy et al. 2022 and 47 "credible" genes from O'Connell et al. 2023. Phosphosites that correlate with homeostatic synaptic scaling were curated from[59], including together all phosphosites that were significantly altered (adjusted *P*-value <0.05) after 5 minutes, 15 minutes or 24 hours of either bicuculline or tetrodotoxin treatment. Curated gene sets that we have previously described[3] include "Activity-regulated genes" (ARGs), which include rapid, delayed and slow primary response genes induced by neuronal depolarization *in vitro* [73], GWAS and exome associations for neuropsychiatric traits[20,74–76], and dopamine-induced genes which are genes with FDR < 0.1 that were upregulated in striatal neuronal culture following 1 hour dopamine treatment[131]. GSEA analysis with custom gene sets was conducted by appending these sets to the C5 MSigDB database. The GSEA results using custom gene sets are available in Supplementary Table 4.

Brain slice electrophysiology

6-8-week-old male and female mice were used for brain slice electrophysiology experiments, including n = 25 slices from 8 mice WT, n = 24 slices from 7 mice *Akap11*$^{+/-}$, and n = 23 slices

from 8 mice *Akap11*$^{-/-}$. An NMDG-based cutting solution was used and contains (in Mm): 93 NMDG, 2.5 KCl, 1.2 NaH_2PO_4, 30 $NaHCO_3$, 20 HEPES, 25 Glucose, 10 $MgSO_4$, 0.5 $CaCl_2$, 5 Sodium Ascorbate, 2 Thiourea, 3 Sodium Pyruvate. pH = 7.3-7.4, OSM = 300-310. The external artificial cerebrospinal fluid (ACSF) recording solution contains(in Mm): 124 NaCl, 2.5 KCl, 1.25 NaH_2PO_4, 24 $NaHCO_3$, 5 HEPES, 12.5 Glucose,1 $MgSO_4$, 2 $CaCl_2$ pH = 7.35, OSM = 300. For brain slice preparation, cardiac perfusion was performed with cold NMDG cutting solution under isoflurane anesthesia. Transverse (horizontal) brain slices containing hippocampus were cut at 400µM with a Leica VT1200S Microtome when submerged in ice-cold NMDG cutting solution. Brain slices were transferred to NMDG solution at 32ºC for approximately 10 min before being transferred to RT brain slice holding solution. Slices were allowed to recover for at least 1 hour before starting the recordings.

To obtain hippocampus field electric postsynaptic potential (EPSP), a concentric bipolar stim electrode (FHC Inc) and a borosilicate glass recording electrode (2-3mOhm resistance) were placed in the classic schaffer collateral to CA1 (SC-CA1) pathway. The signals were low-pass filtered at 2.8kHz using a MultiClamp 700B amplifier (Molecular Devices) and digitized at 10kHz using a DAQ board (National Instrument). Baseline field EPSP were evoked by a paired-pulse stimulation (40ms ISI) every twenty seconds, and a stimulation intensity that evoked 40% of the maximum field EPSP response was used for baseline recording.

For input-output recordings, field EPSP responses were evoked with varying stimulation intensities (20-500 µA). For early LTP recordings, slices were stimulated for approximately 30 mins until a stable baseline field EPSP was obtained. Theta burst stimulation consists of short bursts of 4 stimulation pulses at 10Hz delivered at theta frequency (5Hz, 10 epoches) were used to induce LTP. The field EPSP was recorded for another 20 mins after LTP induction. Paired-pulse ratio was quantified using the field EPSP collected from the 10-minute period before LTP induction and was defined as the ratio between the second and the first field EPSP slope. Field EPSP slope was quantified as the slope during 10-90% of the raise time.

Single-molecule fluorescent in-situ hybridization (smFISH)

Mouse brain characterization of *Akap11*, *Prkaca*, and *Prkar1a* expression was performed using Advanced Cell System's (ACD) single-molecule *in situ* hybridization multiplexed fluorescent amplification kits (ACD catalog numbers 323270). 12-week-old male mice, n=6 per genotype WT, *Akap11*$^{+/-}$, and *Akap11*$^{-/-}$, were deeply anesthetized under isoflurane, perfused with ice-cold HBSS for 3 minutes, and decapitated. Brains were extracted and frozen gradually over liquid nitrogen vapors. Frozen brains were stored in tubes with O.C.T. in -80°c. Brains were sectioned sagittally at 12um/section using a Leica cryostat. Four sections per animal (two sections per slide) were collected on SuperFrost Charged slides and stored at -80ºC and smFISH was performed the following day. Slides were post-fixed in freshly made, pre-chilled 4% PFA (Electron Microscopy Sciences) in PBS for 1 hour on ice. Sections were then dehydrated with 50%, 70%, and 100% ethanol for 5 min at room temperature. All slides were outlined with a grease pen and all following smFISH steps were done on a humidified slide rack. Sections were then treated with hydrogen peroxide for 10 min followed by three PBS washes. Sections then underwent permeabilization with "protease IV" for 30 min followed by three PBS washes.

Sections were then hybridized using probes to *Prkaca* (channel 1), *Akap11* (channel 2), and *Prkar1a* (channel 3) at 40ºC for 2 hours, washed twice with wash buffer, and placed in aluminum foil-wrapped slide holders filled with 5X SSC (Thermo Fisher Scientific, 15557044) overnight at room temperature. The following day, sections were thoroughly washed in wash buffer and probes were amplified using the AMP reagents from the ACD kit. Slides were washed between each step using the wash buffer. HRP binding was also carried out according to the kit's protocol with C1, C2, and C3. Fluorophores were diluted at 1:750 in TSA buffer: C1 was in 488; Channel 2 was in Cy3; Channel 3; Cy5. Once the procedure was completed, slides were counterstained with room temperature Prolong Gold Antifade Mountant with DAPI (Thermo Fisher Scientific, P36935).

Slides were scanned in a Zeiss Axioscan 7 microscope slide scanner with a 40x objective quadruple bandpass filter set with DAPI focus. CZI files were converted to 8-bit TIFF images in FIJI and appropriate brain regions (cortex, thalamus, hippocampus, and striatum) were outlined using the freehand selection tool. To assess levels of *Akap11*, *Prkaca*, and *Prka1a*, the mean intensity was quantified for each outlined brain region with background subtraction using the declive (VI), molecular layer. Four sections per animal were averaged and normalized to the WT to minimize batch effects.

Viruses

FLIM-AKAR and FLIM-AKAR^{T391A} viruses were packaged in-house into a AAV2/AAV9 vector using plasmids that were available from Addgene (no. 60445 and 60446). The final viral constructs and concentration used in this study were: AAV2/1-FLEX-FLIM-AKAR (8.53 × 10^{12}gc/ml), AAV9-FLEX-FLIM-AKAR (2.14 × 10^{13} gc/ml), AAV2-FLEX-FLIM-AKAR^{T391A} (1.23 x 10^13 gc/ml), AAV9-FLEX-FLIM-AKAR^{T391A} (7.67 × 10^{12} gc/ml). AAV2rg-Ef1a-Cre (1.39 × 10^{13} gc/ml) was obtained from Salk institute. While both AAV2 and AAV9 versions of the FLIM-AKAR and FLIM-AKAR^{T391A} were used in this study, we saw no noticeable difference in their expression level and baseline fluorescence lifetime when expressed in wild-type mice. During the experiments, FLIM-AKAR or mutant FLIM-AKAR^{T391A} virus was mixed with the Cre virus in a 4:1 ratio. A final volume of 250 nL was used for intracranial injection.

Stereotaxic Surgery and Virus Injection

Mice were anesthetized with isoflurane and underwent bilateral injection of the virus mix (FLIM-AKAR + Cre or FLIM-AKAR^{T391A} + Cre). Typically, one side of the brain is injected with FLIM-AKAR + Cre, while the other side is injected with FLIM-AKAR^{T391A} + Cre while counterbalancing the sides of the brain, with the exception of twelve mice (mixed genotypes) injected with Dlight 3.8 virus instead of FLIM-AKAR^{T391A} + Cre (data not included). Virus injection was conducted using coordinates for the nucleus accumbens lateral shell (AP +1.20, ML $\pm$1.50 from bregma, DV -4.2 from brain surface). Optical fibers (MFC_200/230-0.37_4.5mm_MF1.25_FLT from Doris Lenses) were placed bilaterally and ~ 0.3 mm above the injection site.

Fluorescence lifetime photometry (FLiP)

Thirty-three 12-20 week-old *Akap11* mutant mice of mixed genotypes were used for stereotaxic surgeries and subsequent FLiP experiments. Approximately equal number of male and female

mice were used. (n=10 WT, n=11 *Akap11*$^{+/-}$ and n=10 *Akap11*$^{-/-}$). The fluorescence lifetime and intensity of the FILM-AKAR (or FLIM-AKAR^{T391A}) was measured in real time at 10kHz using a Fluorescent lifetime photometry system[103]. A customized MATLABM software was used to collect the lifetime measurement, and the lifetime data was down sampled to 10 Hz using a rolling mean. This setup will be described in detail and analysis code will be provided in an upcoming manuscript (Lodder *et al.,* In Preparation).

Animals were habituated into the recording room for at least 30 mins before the experiments. Baseline FLIM-AKAR lifetime was measured for 20 mins during the first measurement, and were then collected for 10 mins each during subsequent measurements, while animals were allowed to freely move in an open field (18x18 cm). Drug injections (dopamine D1/D2 antagonists) during pharmacology experiments were conducted after 10 mins baseline lifetime measurement, and the lifetime data were collected for at least another 20 mins following intraperitoneal injections.

The drugs used in our study include: D1R antagonist (SKF 83566 hydrobromide, Cayman Chemical #29480; 3 mg kg^{-1}), D2R antagonist (eticlopride hydrochloride, Cayman Chemical #29112; 0.5 mg kg^{-1}). Drugs were dissolved in sterile saline at appropriate concentrations and were injected at 0.1 ml solution per 10 g of mouse. An average injection including scruffing the mice took ~30 s and animals were habituated to the injection procedure with sterile saline twice before the pharmacology experiments.

After the FLiP experiments were completed, all mice were perfused transcardially with PFA. Coronal brain sections (80μM) near the optical fiber implants were sliced using a vibratome (Leica VT1200S). The brain slices were mounted with Prolong Gold Antifade Mountant with DAPI (Thermo Fisher Scientific, P36935) and imaged with a Zeiss Axioscan 7 slidescanner.

The experimenter was blinded to the genotype of the mice during the experiments and subsequent data analysis. Two out of thirty-three FLIM-AKAR measurements were excluded from the study due to the low expression of the FILM-AKAR causing the autofluorescent contribution to the recorded lifetime to be greater than 20% based on our estimation. The exclusion criteria was determined before the experiment while the experimenter was still blinded to the mice genotypes.

<u>Amphetamine induced-hyperlocomotion (AIH)</u>

Akap11 mice that were 10-12 weeks old with roughly equal numbers of male and female mice were used for the AIH experiment. n=9 WT, n=11 *Akap11*$^{+/-}$ and n=7 *Akap11*$^{-/-}$ were used for this experiment. Mice in each genotype were randomly assigned to the saline or amphetamine groups. Before the experiment, dextroamphetamine sulfate (Millipore Sigma 1180004; salt corrected) was dissolved in water at 0.2667 mg/mL and was pH corrected to 7.3. Mice were weighted and were allowed to habituate in the behavioral room (under white light) for 30 mins before the start of the experiment. For the measurement of locomotion, mice were placed in Omnitech Electronics Inc SuperFlex Open Field apparatus, which was cleaned with 70%

ethanol between each experiment. First, a 90 min baseline locomotion was recorded, followed by subcutaneous injection of amphetamine at a dose of 2mg/kg or saline. Following drug injection, the locomotion data were collected for another 90 min. Locomotion data were measured by infrared beams and were measured by beam breaks, and were grouped into 5-min bins for analysis.

Accelerating Rotarod

A subset of male and female mice that underwent homecage assay (n= 7 WT, n=6 *Akap11*$^{+/-}$, n=6 *Akap11*$^{-/-}$) were evaluated with the rotarod test (Harvard 76-0770,) when they were 6 months old. Biological sex was approximately evenly split between genotypes. Mice were first allowed to acclimate to the testing room in their home cages for at least 30 minutes prior to beginning testing. Mice underwent 3 training trials where they acclimated to walking on the rotating rod spinning at 4 rotations per minute (rpm). Two mice (n=1 *Akap11*$^{+/-}$, n=1 *Akap11*$^{-/-}$) were excluded from testing because they fell off immediately during all three training trials. Mice then underwent 4 test trials, with at least 1 minute between trials, where the rod accelerated at a constant rate from an initial speed of 4rpm until the mouse was unable to keep pace with the rotations and fell off of the rotating bar, or until a maximum speed of 40 rpm. This latency to fall was recorded and the data is shown as the average of 4 test trials.

Homecage locomotor activity monitoring

Male and female mice aged P23-P34 were transferred to Digital Ventilated Cages (DVC, Tecniplast) and were single housed throughout the duration of the experiment. Briefly, DVC racks use 12 electrodes beneath each cage that radiates an electromagnetic field that can detect disturbances that correlate with animal movement. The DVC Analytics web platform was used to generate animal locomotor indices, which calculate the percentage of 12 electrodes that measured movement over a 1-minute bin. For the locomotor activity index, a value of 1 means 12 electrodes measured movement, and a value greater than 1 means that there were > 12 detected movements. n = 20 females and 15 males were used for the experiment, including n=11 WT, n=13 *Akap11*$^{+/-}$ and n=11 *Akap11*$^{-/-}$. The sex distribution was roughly equal across genotypes.

Behavioral Battery (sucrose preference test, forced swim test, and prepulse inhibition)

Fifty-five AKAP11 mice (n=19 WT, n=22 *Akap11*$^{+/-}$, n=14 *Akap11*$^{-/-}$) aged between 12-16 weeks were used in a battery of behavioral assays including sucrose preference test, forced swim test, and prepulse inhibition. Animals were grouped housed in a maximum of 5 animals per cage, under normal lighting (lights on 7am-7pm) and ad libitum supply of food and water. All procedures were approved by the Institutional Animal Care and Use Committee at Boston Children's Hospital and were in accordance with the National Institutes of Health Guide for the Care and Use of Laboratory Animals.

For the sucrose preference test: on day 1, mice were individually housed and were habituated to 2% sucrose for 24 hours. All bottles were pre-weighed and each mouse got two bottles filled with 2% sucrose solution. The bottles are retrieved and weighed at the end of the habituation day. On day 2 and 3, mice were individually housed and underwent a sucrose preference test.

One of the bottles was filled with 2% sucrose solution while the other was filled with water. The position of the sucrose/water bottle was reversed at the end of day 2, and the bottles were weighed at the end of each day to determine water/sucrose consumption. Sucrose preference test was conducted once at the beginning of the behavioral test battery and was repeated once after other behavioral assays (forced swim test and prepulse inhibition) were completed. The experimenter was blinded to the genotype of the test mice throughout the experiment.

For the forced swim test, mice were habituated to the behavioral room 30 mins prior to the experiment. A 4L beaker was filled 2/3 of the way with water and was maintained at room temperature (24°C ± 1°C), measured before each experiment with a glass thermometer. Mice were gently placed in water and were closely observed throughout the 6-min test. Mice were immediately removed if they were unable to keep their head above water. After the test, mice were gently dried with a paper towel and were allowed to recover in the home cage for 10 mins under monitoring. Time immobile was manually scored with a stopwatch by an experimenter blinding to the animal genotype.

For prepulse inhibition, mice were habituated to the behavioral room 30 mins prior to the start of the experiment. During the experiments, mice were allowed mins to acclimate to the 60 db background noise that was present throughout the experiment. Mice were presented with 4 variable auditory pre-pulse levels (70, 74, 78, 82 dV; 20ms), followed by an auditory startle pulse (110 dB, 20ms) 100ms after the pre-pulse. A total of 20 trials is delivered for each mouse (5 repeats for each of the 4 pre-pulse levels) in a random order with a variable inter-trial-interval ranging from 10-30 seconds. The startle response was measured during the 250ms period after the onset of the startle pulse by a force meter (Kinder Scientific). The percentage of prepulse inhibition is quantified by the following equation: %PPI = 100 × [(pulse-alone) – (pre-pulse + pulse score)]/pulse-alone score.

Statistics

Statistics for immunoblots, fluorescence lifetime photometry (FLiP), and behavior were calculated in GraphPad Prism, with each dot representing an individual animal. Immunoblots and FLiP experiments including the genotype factor and a second factor (Age, Brain region, Protein interactor, or FLIM-AKAR variant) were quantified with two-way ANOVA. For all analyses with a significant main effect of genotype, post hoc Tukey's multiple comparisons were conducted for all possible comparisons within the same level of the second factor (e.g. WT, *Akap11*$^{+/-}$ and *Akap11*$^{-/-}$ were compared within one age, but not between different ages). Multiple comparisons were conducted with Tukey's post hoc test. For Extended Data Figs. 2b,c and 3g, where *Akap11*$^{-/-}$ was excluded, Sidak's multiple comparisons test was used. For immunoblot, behavioral, and FLiP experiments where genotype was the only variable, statistically analysis were conducted by one-way ANOVA followed by Tukey's post hoc test to compare all genotype pairs.

Data availability

The original mass spectra and the protein sequence database used for searches have been deposited in the public proteomics repository MassIVE (http://massive.ucsd.edu)

and are accessible at ftp://MSV000095852@massive.ucsd.edu. These datasets will be made public upon acceptance of the manuscript. Processed and raw bulk and single nucleus RNAsequencing data have been deposited at GEO with the following IDs: bulk RNAseq: GSE272097. single nucleus RNAseq: GSE272098. For transcriptome analyses of *Akap11* abundance in wild-type mice, the following publicly available datasets were analyzed: GSE218573. All software used in the analysis are publicly available.

References

1. Singh, T. *et al.* Rare coding variants in ten genes confer substantial risk for schizophrenia. *Nature* **604**, 509–516 (2022).
2. Palmer, D. S. *et al.* Exome sequencing in bipolar disorder identifies AKAP11 as a risk gene shared with schizophrenia. *Nat. Genet.* **54**, 541–547 (2022).
3. Farsi, Z. *et al.* Brain-region-specific changes in neurons and glia and dysregulation of dopamine signaling in Grin2a mutant mice. *Neuron* **111**, 3378–3396.e9 (2023).
4. Farsi, Z. & Sheng, M. Molecular mechanisms of schizophrenia: Insights from human genetics. *Curr. Opin. Neurobiol.* **81**, 102731 (2023).
5. Nakamura, T. & Takata, A. The molecular pathology of schizophrenia: an overview of existing knowledge and new directions for future research. *Mol. Psychiatry* **28**, 1868–1889 (2023).
6. Liu, D. *et al.* Schizophrenia risk conferred by rare protein-truncating variants is conserved across diverse human populations. *Nat. Genet.* **55**, 369–376 (2023).
7. Herzog, L. E. *et al.* Mouse mutants in schizophrenia risk genes GRIN2A and AKAP11 show EEG abnormalities in common with schizophrenia patients. *Transl. Psychiatry* **13**, 92 (2023).
8. Wong, W. & Scott, J. D. AKAP signalling complexes: focal points in space and time. *Nat. Rev. Mol. Cell Biol.* **5**, 959–970 (2004).
9. Day, M. E. *et al.* Isoform-specific targeting of PKA to multivesicular bodies. *J. Cell Biol.* **193**, 347–363 (2011).
10. Lester, L. B., Coghlan, V. M., Nauert, B. & Scott, J. D. Cloning and Characterization of a Novel A-kinase Anchoring Protein: AKAP 220, ASSOCIATION WITH TESTICULAR PEROXISOMES (∗). *J. Biol. Chem.* **271**, 9460–9465 (1996).
11. Tanji, C. *et al.* A-kinase anchoring protein AKAP220 binds to glycogen synthase kinase-3beta (GSK-3beta) and mediates protein kinase A-dependent inhibition of GSK-3beta. *J. Biol. Chem.* **277**, 36955–36961 (2002).
12. Schillace, R. V. & Scott, J. D. Association of the type 1 protein phosphatase PP1 with the A-kinase anchoring protein AKAP220. *Curr. Biol.* **9**, 321–324 (1999).
13. Logue, J. S. *et al.* AKAP220 protein organizes signaling elements that impact cell migration. *J. Biol. Chem.* **286**,

39269–39281 (2011).

14. Yang, L., Nakayama, Y., Hattori, N., Liu, B. & Inagaki, C. GABAC-Receptor Stimulation Activates cAMP-Dependent Protein Kinase via A-Kinase Anchoring Protein 220. *J. Pharmacol. Sci.* **106**, 578–584 (2008).
15. Mikitova, V. & Levine, T. P. Analysis of the key elements of FFAT-like motifs identifies new proteins that potentially bind VAP on the ER, including two AKAPs and FAPP2. *PLoS One* **7**, e30455 (2012).
16. Deng, Z. *et al.* Selective autophagy of AKAP11 activates cAMP/PKA to fuel mitochondrial metabolism and tumor cell growth. *Proc. Natl. Acad. Sci. U. S. A.* **118**, (2021).
17. Whiting, J. L. *et al.* AKAP220 manages apical actin networks that coordinate aquaporin-2 location and renal water reabsorption. *Proc. Natl. Acad. Sci. U. S. A.* **113**, E4328–37 (2016).
18. Whiting, J. L. *et al.* Protein Kinase A Opposes the Phosphorylation-dependent Recruitment of Glycogen Synthase Kinase 3β to A-kinase Anchoring Protein 220*. *J. Biol. Chem.* **290**, 19445–19457 (2015).
19. Dema, A. *et al.* The A-Kinase Anchoring Protein (AKAP) Glycogen Synthase Kinase 3β Interaction Protein (GSKIP) Regulates β-Catenin through Its Interactions with Both Protein Kinase A (PKA) and GSK3β *. *J. Biol. Chem.* **291**, 19618–19630 (2016).
20. Satterstrom, F. K. *et al.* Large-Scale Exome Sequencing Study Implicates Both Developmental and Functional Changes in the Neurobiology of Autism. *Cell* **180**, 568–584.e23 (2020).
21. Shih, Y.-T., Alipio, J. B. & Sahay, A. An inhibitory circuit-based enhancer of DYRK1A function reverses Dyrk1a-associated impairment in social recognition. *Neuron* **111**, 3084–3101.e5 (2023).
22. Dang, T. *et al.* Autism-associated Dyrk1a truncation mutants impair neuronal dendritic and spine growth and interfere with postnatal cortical development. *Mol. Psychiatry* **23**, 747–758 (2018).
23. Levy, J. A., LaFlamme, C. W., Tsaprailis, G., Crynen, G. & Page, D. T. Dyrk1a Mutations Cause Undergrowth of Cortical Pyramidal Neurons via Dysregulated Growth Factor Signaling. *Biol. Psychiatry* **90**, 295–306 (2021).
24. Arranz, J. *et al.* Impaired development of neocortical circuits contributes to the neurological alterations in DYRK1A haploinsufficiency syndrome. *Neurobiol. Dis.* **127**, 210–222 (2019).
25. Subramanian, A. *et al.* Gene set enrichment analysis: A knowledge-based approach for interpreting genome-wide expression profiles. *Proceedings of the National Academy of Sciences* **102**, 15545–15550 (2005).
26. Nikom, D. & Zheng, S. Alternative splicing in neurodegenerative disease and the promise of RNA therapies. *Nat. Rev. Neurosci.* **24**, 457–473 (2023).
27. Paulussen, I. *et al.* SV2B defines a subpopulation of synaptic vesicles. *J. Mol. Cell Biol.* (2023) doi:10.1093/jmcb/mjad054.
28. Vierra, N. C. *et al.* Neuronal ER-plasma membrane junctions couple excitation to Ca2+-activated PKA signaling.

Nat. Commun. **14**, 1–16 (2023).

29. Parzych, K. R. & Klionsky, D. J. An overview of autophagy: morphology, mechanism, and regulation. *Antioxid. Redox Signal.* **20**, 460–473 (2014).
30. Zhou, X. *et al.* Integrated proteomics reveals autophagy landscape and an autophagy receptor controlling PKA-RI complex homeostasis in neurons. *Nat. Commun.* **15**, 1–18 (2024).
31. Segura-Roman, A. *et al.* Autophagosomes coordinate an AKAP11-dependent regulatory checkpoint that shapes neuronal PKA signaling. *bioRxiv* 2024.08.06.606738 (2024) doi:10.1101/2024.08.06.606738.
32. Kandel, E. R. The molecular biology of memory: cAMP, PKA, CRE, CREB-1, CREB-2, and CPEB. *Mol. Brain* **5**, 14 (2012).
33. Solmi, M. *et al.* Age at onset of mental disorders worldwide: large-scale meta-analysis of 192 epidemiological studies. *Mol. Psychiatry* **27**, 281–295 (2022).
34. Darling, N. J. & Cohen, P. Nuts and bolts of the salt-inducible kinases (SIKs). *Biochem. J* **478**, 1377–1397 (2021).
35. Yamada, T., Sakisaka, T., Hisata, S., Baba, T. & Takai, Y. RA-RhoGAP, Rap-activated Rho GTPase-activating protein implicated in neurite outgrowth through Rho. *J. Biol. Chem.* **280**, 33026–33034 (2005).
36. Aryal, S. *et al.* Deep proteomics identifies shared molecular pathway alterations in synapses of patients with schizophrenia and bipolar disorder and mouse model. *Cell Rep.* **42**, 112497 (2023).
37. Koopmans, F. *et al.* SynGO: An Evidence-Based, Expert-Curated Knowledge Base for the Synapse. *Neuron* **103**, 217–234.e4 (2019).
38. Myles-Worsley, M. *et al.* Deletion at the SLC1A1 glutamate transporter gene co-segregates with schizophrenia and bipolar schizoaffective disorder in a 5-generation family. *Am. J. Med. Genet. B Neuropsychiatr. Genet.* **162B**, 87–95 (2013).
39. Stefansson, H. *et al.* Neuregulin 1 and susceptibility to schizophrenia. *Am. J. Hum. Genet.* **71**, 877–892 (2002).
40. Hornbeck, P. V. *et al.* PhosphoSitePlus, 2014: mutations, PTMs and recalibrations. *Nucleic Acids Res.* **43**, D512–20 (2015).
41. Bramson, H. N., Kaiser, E. T. & Mildvan, A. S. Mechanistic studies of cAMP-dependent protein kinase action. *CRC Crit. Rev. Biochem.* **15**, 93–124 (1984).
42. Krug, K. *et al.* A Curated Resource for Phosphosite-specific Signature Analysis. *Mol. Cell. Proteomics* **18**, 576–593 (2019).
43. Lisman, J., Yasuda, R. & Raghavachari, S. Mechanisms of CaMKII action in long-term potentiation. *Nat. Rev. Neurosci.* **13**, 169–182 (2012).

44. Liu, C. *et al.* Control of beta-catenin phosphorylation/degradation by a dual-kinase mechanism. *Cell* **108**, 837–847 (2002).

45. Amit, S. *et al.* Axin-mediated CKI phosphorylation of beta-catenin at Ser 45: a molecular switch for the Wnt pathway. *Genes Dev.* **16**, 1066–1076 (2002).

46. Fang, X. *et al.* Phosphorylation and inactivation of glycogen synthase kinase 3 by protein kinase A. *Proc. Natl. Acad. Sci. U. S. A.* **97**, 11960–11965 (2000).

47. Malhi, G. S., Gessler, D. & Outhred, T. The use of lithium for the treatment of bipolar disorder: Recommendations from clinical practice guidelines. *J. Affect. Disord.* **217**, 266–280 (2017).

48. Nakao, K. *et al.* GSK3β inhibition restores cortical gamma oscillation and cognitive behavior in a mouse model of NMDA receptor hypofunction relevant to schizophrenia. *Neuropsychopharmacology* **45**, 2207–2218 (2020).

49. Banke, T. G. *et al.* Control of GluR1 AMPA receptor function by cAMP-dependent protein kinase. *J. Neurosci.* **20**, 89–102 (2000).

50. Ehlers, M. D. Reinsertion or degradation of AMPA receptors determined by activity-dependent endocytic sorting. *Neuron* **28**, 511–525 (2000).

51. Esteban, J. A. *et al.* PKA phosphorylation of AMPA receptor subunits controls synaptic trafficking underlying plasticity. *Nat. Neurosci.* **6**, 136–143 (2003).

52. Diering, G. H., Gustina, A. S. & Huganir, R. L. PKA-GluA1 coupling via AKAP5 controls AMPA receptor phosphorylation and cell-surface targeting during bidirectional homeostatic plasticity. *Neuron* **84**, 790–805 (2014).

53. Huganir, R. L. & Nicoll, R. A. AMPARs and synaptic plasticity: the last 25 years. *Neuron* **80**, 704–717 (2013).

54. Nagy, G. *et al.* Regulation of releasable vesicle pool sizes by protein kinase A-dependent phosphorylation of SNAP-25. *Neuron* **41**, 417–429 (2004).

55. Simsek-Duran, F., Linden, D. J. & Lonart, G. Adapter protein 14-3-3 is required for a presynaptic form of LTP in the cerebellum. *Nat. Neurosci.* **7**, 1296–1298 (2004).

56. Lonart, G. *et al.* Phosphorylation of RIM1alpha by PKA triggers presynaptic long-term potentiation at cerebellar parallel fiber synapses. *Cell* **115**, 49–60 (2003).

57. Kaeser, P. S. *et al.* RIM1alpha phosphorylation at serine-413 by protein kinase A is not required for presynaptic long-term plasticity or learning. *Proc. Natl. Acad. Sci. U. S. A.* **105**, 14680–14685 (2008).

58. Betzenhauser, M. J., Fike, J. L., Wagner, L. E., 2nd & Yule, D. I. Protein kinase A increases type-2 inositol 1,4,5-trisphosphate receptor activity by phosphorylation of serine 937. *J. Biol. Chem.* **284**, 25116–25125 (2009).

59. Desch, K., Langer, J. D. & Schuman, E. M. Dynamic bi-directional phosphorylation events associated with the

reciprocal regulation of synapses during homeostatic up- and down-scaling. *Cell Rep.* **36**, 109583 (2021).

60. Diering, G. H. & Huganir, R. L. The AMPA Receptor Code of Synaptic Plasticity. *Neuron* **100**, 314–329 (2018).
61. Makino, Y., Johnson, R. C., Yu, Y., Takamiya, K. & Huganir, R. L. Enhanced synaptic plasticity in mice with phosphomimetic mutation of the GluA1 AMPA receptor. *Proceedings of the National Academy of Sciences* **108**, 8450–8455 (2011).
62. Biederbick, A., Rose, S. & Elsässer, H. P. A human intracellular apyrase-like protein, LALP70, localizes to lysosomal/autophagic vacuoles. *J. Cell Sci.* **112 (Pt 15)**, 2473–2484 (1999).
63. Astori, S. *et al.* The Ca(V)3.3 calcium channel is the major sleep spindle pacemaker in thalamus. *Proc. Natl. Acad. Sci. U. S. A.* **108**, 13823–13828 (2011).
64. Ghoshal, A. *et al.* Effects of a patient-derived de novo coding alteration of CACNA1I in mice connect a schizophrenia risk gene with sleep spindle deficits. *Transl. Psychiatry* **10**, 29 (2020).
65. Kozhemiako, N. *et al.* Non-rapid eye movement sleep and wake neurophysiology in schizophrenia. *bioRxiv* 2021.12.13.472475 (2021) doi:10.1101/2021.12.13.472475.
66. Dejanovic, B., Sheng, M. & Hanson, J. E. Targeting synapse function and loss for treatment of neurodegenerative diseases. *Nat. Rev. Drug Discov.* **23**, 23–42 (2024).
67. Schizophrenia Working Group of the Psychiatric Genomics Consortium. Biological insights from 108 schizophrenia-associated genetic loci. *Nature* **511**, 421–427 (2014).
68. Sekar, A. *et al.* Schizophrenia risk from complex variation of complement component 4. *Nature* **530**, 177–183 (2016).
69. Gandal, M. J. *et al.* Transcriptome-wide isoform-level dysregulation in ASD, schizophrenia, and bipolar disorder. *Science* **362**, eaat8127 (2018).
70. Ruzicka, B. *et al.* Single-Cell Dissection of Schizophrenia Reveals Neurodevelopmental-Synaptic Link and Transcriptional Resilience Associated Cellular State. *Biol. Psychiatry* **89**, S106 (2021).
71. Minzenberg, M. J., Laird, A. R., Thelen, S., Carter, C. S. & Glahn, D. C. Meta-analysis of 41 functional neuroimaging studies of executive function in schizophrenia. *Arch. Gen. Psychiatry* **66**, 811–822 (2009).
72. Chen, C.-H., Suckling, J., Lennox, B. R., Ooi, C. & Bullmore, E. T. A quantitative meta-analysis of fMRI studies in bipolar disorder: Meta-analysis of fMRI studies in BD. *Bipolar Disord.* **13**, 1–15 (2011).
73. Tyssowski, K. M. *et al.* Different Neuronal Activity Patterns Induce Different Gene Expression Programs. *Neuron* **98**, 530–546.e11 (2018).
74. Buniello, A. *et al.* The NHGRI-EBI GWAS Catalog of published genome-wide association studies, targeted arrays and summary statistics 2019. *Nucleic Acids Res.* **47**, D1005–D1012 (2019).

75. Kaplanis, J. *et al.* Evidence for 28 genetic disorders discovered by combining healthcare and research data. *Nature* **586**, 757–762 (2020).

76. International League Against Epilepsy Consortium on Complex Epilepsies. Genome-wide mega-analysis identifies 16 loci and highlights diverse biological mechanisms in the common epilepsies. *Nat. Commun.* **9**, 5269 (2018).

77. Cross-Disorder Group of the Psychiatric Genomics Consortium. Genomic Relationships, Novel Loci, and Pleiotropic Mechanisms across Eight Psychiatric Disorders. *Cell* **179**, 1469–1482.e11 (2019).

78. Trubetskoy, V. *et al.* Mapping genomic loci implicates genes and synaptic biology in schizophrenia. *Nature* **604**, 502–508 (2022).

79. O'Connell, K. S. *et al.* Genetic diversity enhances gene discovery for bipolar disorder. *medRxiv* 2023.10.07.23296687 (2023) doi:10.1101/2023.10.07.23296687.

80. Ling, E. *et al.* A concerted neuron–astrocyte program declines in ageing and schizophrenia. *Nature* **627**, 604–611 (2024).

81. Glennon, R. A., Titeler, M. & McKenney, J. D. Evidence for 5-HT2 involvement in the mechanism of action of hallucinogenic agents. *Life Sci.* **35**, 2505–2511 (1984).

82. López-Giménez, J. F. & González-Maeso, J. Hallucinogens and serotonin 5-HT2A receptor-mediated signaling pathways. *Curr. Top. Behav. Neurosci.* **36**, 45–73 (2018).

83. Cookson, J. & Jonsson, F. A new cholinergic mechanism for antipsychotics: emraclidine and M4 muscarinic receptors. *Lancet* **400**, 2159–2161 (2022).

84. Kaul, I. *et al.* Efficacy and safety of the muscarinic receptor agonist KarXT (xanomeline–trospium) in schizophrenia (EMERGENT-2) in the USA: results from a randomised, double-blind, placebo-controlled, flexible-dose phase 3 trial. *Lancet* **403**, 160–170 (2024).

85. Shamah, S. M. *et al.* EphA Receptors Regulate Growth Cone Dynamics through the Novel Guanine Nucleotide Exchange Factor Ephexin. *Cell* **105**, 233–244 (2001).

86. Frisén, J., Holmberg, J. & Barbacid, M. Ephrins and their Eph receptors: multitalented directors of embryonic development. *EMBO J.* **18**, 5159–5165–5165 (1999).

87. Williams, M. E. *et al.* Cadherin-9 regulates synapse-specific differentiation in the developing hippocampus. *Neuron* **71**, 640–655 (2011).

88. García, M. *et al.* The syndrome of central hypothyroidism and macroorchidism: IGSF1 controls TRHR and FSHB expression by differential modulation of pituitary TGFβ and Activin pathways. *Sci. Rep.* **7**, 42937 (2017).

89. Joustra, S. D. *et al.* IGSF1 deficiency syndrome: A newly uncovered endocrinopathy. *Rare Dis* **1**, e24883 (2013).

90. Chakrabarti, S. Thyroid functions and bipolar affective disorder. *J. Thyroid Res.* **2011**, 306367 (2011).

91. Gerfen, C. R. Segregation of D1 and D2 dopamine receptors in the striatal direct and indirect pathways: An historical perspective. *Front. Synaptic Neurosci.* **14**, 1002960 (2022).

92. Lew, J. Y. *et al.* Increased site-specific phosphorylation of tyrosine hydroxylase accompanies stimulation of enzymatic activity induced by cessation of dopamine neuronal activity. *Mol. Pharmacol.* **55**, 202–209 (1999).

93. Lindgren, N. *et al.* Regulation of tyrosine hydroxylase activity and phosphorylation at Ser(19) and Ser(40) via activation of glutamate NMDA receptors in rat striatum. *J. Neurochem.* **74**, 2470–2477 (2000).

94. Nagai, T. *et al.* Phosphoproteomics of the Dopamine Pathway Enables Discovery of Rap1 Activation as a Reward Signal In Vivo. *Neuron* **89**, 550–565 (2016).

95. Kimmel, H. L., Gong, W., Vechia, S. D., Hunter, R. G. & Kuhar, M. J. Intra-ventral tegmental area injection of rat cocaine and amphetamine-regulated transcript peptide 55-102 induces locomotor activity and promotes conditioned place preference. *J. Pharmacol. Exp. Ther.* **294**, 784–792 (2000).

96. Hubert, G. W., Jones, D. C., Moffett, M. C., Rogge, G. & Kuhar, M. J. CART peptides as modulators of dopamine and psychostimulants and interactions with the mesolimbic dopaminergic system. *Biochem. Pharmacol.* **75**, 57–62 (2008).

97. Chen, Y., Saulnier, J. L., Yellen, G. & Sabatini, B. L. A PKA activity sensor for quantitative analysis of endogenous GPCR signaling via 2-photon FRET-FLIM imaging. *Front. Pharmacol.* **5**, 56 (2014).

98. Lee, S. J., Chen, Y., Lodder, B. & Sabatini, B. L. Monitoring Behaviorally Induced Biochemical Changes Using Fluorescence Lifetime Photometry. *Front. Neurosci.* **13**, 766 (2019).

99. Jentsch, J. D., Roth, R. H. & Taylor, J. R. Role for dopamine in the behavioral functions of the prefrontal corticostriatal system: implications for mental disorders and psychotropic drug action. *Prog. Brain Res.* **126**, 433–453 (2000).

100. Grace, A. A. Dysregulation of the dopamine system in the pathophysiology of schizophrenia and depression. *Nat. Rev. Neurosci.* **17**, 524–532 (2016).

101. Thomas, E. A. Molecular profiling of antipsychotic drug function: convergent mechanisms in the pathology and treatment of psychiatric disorders. *Mol. Neurobiol.* **34**, 109–128 (2006).

102. Aringhieri, S. *et al.* Molecular targets of atypical antipsychotics: From mechanism of action to clinical differences. *Pharmacol. Ther.* **192**, 20–41 (2018).

103. Lee, S. J. *et al.* Cell-type-specific asynchronous modulation of PKA by dopamine in learning. *Nature* **590**, 451–456 (2021).

104. Graybiel, A. M. & Grafton, S. T. The striatum: where skills and habits meet. *Cold Spring Harb. Perspect. Biol.* **7**,

a021691 (2015).

105. Breier, A. *et al.* Schizophrenia is associated with elevated amphetamine-induced synaptic dopamine concentrations: evidence from a novel positron emission tomography method. *Proc. Natl. Acad. Sci. U. S. A.* **94**, 2569–2574 (1997).

106. Voikar, V. & Gaburro, S. Three Pillars of Automated Home-Cage Phenotyping of Mice: Novel Findings, Refinement, and Reproducibility Based on Literature and Experience. *Front. Behav. Neurosci.* **14**, 575434 (2020).

107. Sherwin, C. M. Voluntary wheel running: a review and novel interpretation. *Anim. Behav.* **56**, 11–27 (1998).

108. Meijer, J. H. & Robbers, Y. Wheel running in the wild. *Proceedings of the Royal Society B: Biological Sciences* **281**, 20140210 (2014).

109. Armario, A. The forced swim test: Historical, conceptual and methodological considerations and its relationship with individual behavioral traits. *Neurosci. Biobehav. Rev.* **128**, 74–86 (2021).

110. Liu, M.-Y. *et al.* Sucrose preference test for measurement of stress-induced anhedonia in mice. *Nat Protoc* **13**, 1686–1698 (2018).

111. Chen, R. *et al.* Cell type-specific mechanism of Setd1a heterozygosity in schizophrenia pathogenesis. *Sci Adv* **8**, eabm1077 (2022).

112. Katrancha, S. M. *et al.* Trio Haploinsufficiency Causes Neurodevelopmental Disease-Associated Deficits. *Cell Rep.* **26**, 2805–2817.e9 (2019).

113. Dejanovic, B. *et al.* Changes in the Synaptic Proteome in Tauopathy and Rescue of Tau-Induced Synapse Loss by C1q Antibodies. *Neuron* **100**, 1322–1336.e7 (2018).

114. Dejanovic, B. *et al.* Complement C1q-dependent excitatory and inhibitory synapse elimination by astrocytes and microglia in Alzheimer's disease mouse models. *Nat Aging* **2**, 837–850 (2022).

115. UniProt Consortium. UniProt: the universal protein knowledgebase in 2021. *Nucleic Acids Res.* **49**, D480–D489 (2021).

116. Zhou, X. L. *et al.* ROR2 modulates neuropathic pain via phosphorylation of NMDA receptor subunit GluN2B in rats. *Br. J. Anaesth.* **123**, e239–e248 (2019).

117. Morshed, N. *et al.* Phosphoproteomics identifies microglial Siglec-F inflammatory response during neurodegeneration. *Mol. Syst. Biol.* **16**, e9819 (2020).

118. O'Shea, J. P. *et al.* pLogo: a probabilistic approach to visualizing sequence motifs. *Nat. Methods* **10**, 1211–1212 (2013).

119. Biancalani, T. *et al.* Deep learning and alignment of spatially resolved single-cell transcriptomes with Tangram.

Nat. Methods **18**, 1352–1362 (2021).

120. Li, B. & Dewey, C. N. RSEM: accurate transcript quantification from RNA-Seq data with or without a reference genome. *BMC Bioinformatics* **12**, 323 (2011).

121. Love, M. I., Huber, W. & Anders, S. Moderated estimation of fold change and dispersion for RNA-seq data with DESeq2. *Genome Biol.* **15**, 550 (2014).

122. Zheng, G. X. Y. *et al.* Massively parallel digital transcriptional profiling of single cells. *Nat. Commun.* **8**, 1–12 (2017).

123. Stuart, T. *et al.* Comprehensive Integration of Single-Cell Data. *Cell* **177**, 1888–1902.e21 (2019).

124. Wolock, S. L., Lopez, R. & Klein, A. M. Scrublet: Computational Identification of Cell Doublets in Single-Cell Transcriptomic Data. *Cell Syst* **8**, 281–291.e9 (2019).

125. Ding, J. *et al.* Systematic comparison of single-cell and single-nucleus RNA-sequencing methods. *Nat. Biotechnol.* **38**, 737–746 (2020).

126. Zeisel, A. *et al.* Molecular Architecture of the Mouse Nervous System. *Cell* **174**, 999–1014.e22 (2018).

127. Saunders, A. *et al.* Molecular Diversity and Specializations among the Cells of the Adult Mouse Brain. *Cell* **174**, 1015–1030.e16 (2018).

128. Leek, J. T., Johnson, W. E., Parker, H. S., Jaffe, A. E. & Storey, J. D. The sva package for removing batch effects and other unwanted variation in high-throughput experiments. *Bioinformatics* **28**, 882–883 (2012).

129. Robinson, M. D., McCarthy, D. J. & Smyth, G. K. edgeR: a Bioconductor package for differential expression analysis of digital gene expression data. *Bioinformatics* **26**, 139–140 (2010).

130. Phipson, B. *et al.* propeller: testing for differences in cell type proportions in single cell data. *Bioinformatics* **38**, 4720–4726 (2022).

131. Savell, K. E. *et al.* A dopamine-induced gene expression signature regulates neuronal function and cocaine response. *Sci Adv* **6**, eaba4221 (2020).